

Magnetic Fields in Star-Forming Molecular Clouds III. Submillimeter Polarimetry of Intermediate Mass Cores and Filaments in Orion B

Brenda C. Matthews

Department of Physics and Astronomy, McMaster University, Hamilton, ON, Canada L8S 4M1

matthews@physics.mcmaster.ca

1

Jason D. Fiege

Canadian Institute for Theoretical Astrophysics, University of Toronto, Toronto, ON, Canada M5S 3H3

fiege@cita.utoronto.ca

and

Gerald Moriarty-Schieven

National Research Council of Canada, Joint Astronomy Centre, Hilo, HI U.S.A. 96720

g.moriarty-schieven@jach.hawaii.edu

ABSTRACT

Using the imaging polarimeter for the Submillimeter Common User Bolometric Array at the James Clerk Maxwell Telescope, we have detected polarized thermal emission at $850\ \mu\text{m}$ from dust toward three star-forming core systems in the Orion B molecular cloud: NGC 2071, NGC 2024 and LBS 23N (HH 24). The polarization patterns are not indicative of those expected for magnetic fields dominated by a single field direction, and all exhibit diminished polarization percentages toward the highest intensity peaks. NGC 2024 has the most organized polarization pattern which is centered consistently along the length of a chain of 7 far-infrared sources. We have modeled NGC 2024 using a helical field geometry threading a curved filament and also as a magnetic field swept up by the ionization front of the expanding H II region. In the latter case, the field is bent by the dense ridge, which accounts for both the polarization pattern and existing measurements of the line-of-sight field strength toward the northern cores FIR 1 to FIR 4. The direction of the net magnetic field direction within NGC 2071 is perpendicular to the dominant outflow in that region. Despite evidence that line contamination exists in the $850\ \mu\text{m}$ continuum, the levels of polarization measured indicate that the polarized emission is dominated by dust.

Subject headings: ISM:clouds – ISM:magnetic fields – polarization – stars:formation – submillimeter

1. Introduction

The Orion B (L1630) molecular cloud, at a distance of 415 pc (Anthony-Twarog 1982), is one of

the nearest giant molecular clouds and is an active site of low- to high-mass star formation. It was one of the first clouds to be systematically studied for dense cores by Lada et al. (1991a), who found that massive star formation takes place only in the five largest clumps, which together make up more than 50% of the mass of dense gas. We have cho-

¹Current address: Dept. of Astronomy, UC, Berkeley
bmatthews@astro.berkeley.edu

sen three of these five clumps, NGC 2071IR (LBS 8), NGC 2024 (LBS 33), and HH24 (LBS 23), for the current study. A fourth region, NGC 2068, contains a string of substantially smaller, fainter cores connected by weak dusty filaments (Mitchell et al. 2001). Polarimetry of this region will be presented in a forthcoming paper (Matthews & Wilson 2001, Paper IV in this series).

Although the three regions have comparable gas masses, ranging from $230\text{-}460 M_{\odot}$ (Lada et al. 1991a), they have very different star formation properties. NGC 2071IR lies four arcminutes north of the reflection nebula NGC 2071. This extended submillimeter source consists of a cluster of at least nine embedded infrared stars (Walther et al. 1993) with a combined infrared luminosity of $520 L_{\odot}$ (Butner et al. 1990). The source IRS 3 is thought to be the driving source of a massive bipolar molecular outflow (Bally 1982; Snell et al. 1984; Moriarty-Schieven, Snell & Hughes 1989; Eislöffel 2000). Houde et al. (2001) infer alignment between the outflow and its magnetic field by comparison of spectral lines of neutral and ionic species. Shocked molecular hydrogen (Bally & Lane 1982) and H_2O masers (Genzel & Downes 1979) are also seen towards this region, which is in a later evolutionary stage than NGC 2024 (Launhardt et al. 1996). Eislöffel (2000) has also documented several other outflows in the region. Submillimeter maps of this region have been published by several authors (Mitchell et al. 2001; Motte et al. 2001; Johnstone et al. 2001). Based on a comparison between submillimeter continuum and CO(3-2) and HCO^+ line data, Motte et al. (2001) suggest that $> 20\%$ of the $850 \mu\text{m}$ emission in the outflow region could originate from line contamination.

By contrast with the other two regions, the HH 24-26 (LBS 23) cores have relatively little extended submillimeter emission and are mostly compact (Mitchell et al. 2001; Johnstone et al. 2001; Launhardt et al. 1996; Lis, Menten & Zylka 1999) and cold ($< 10\text{K}$, Chini et al. (1993)). Of the twelve condensations identified by Lis, Menten & Zylka (1999), our polarimetric image covers LMZ 2, 3, and 4. All three of these cores have 3.6 cm continuum sources (Bontemps, André & Ward-Thompson 1995; Gibb 1999). LMZ 3 (also known as HH24MMS, Chini et al. (1993)) is a class 0 protostar (Bontemps, André & Ward-Thompson

1995), while LMZ 4 is a T Tauri star with a known CO outflow (Snell & Edwards 1982; Gibb & Heaton 1993). These are all indicators of low-mass star formation.

NGC 2024 has an associated H II region and is the most prominent star formation region in Orion B, associated with a massive cluster, ionizing B stars, and stars at all phases of evolution (Mezger et al. 1988; Lada et al. 1991b; Chandler & Carlstrom 1996). The submillimeter continuum emission was discovered by Mezger et al. (1988). The emission arises from a dense ridge of gas and dust behind the H II region, determined from the velocity of associated gas (Crutcher et al. 1986; Barnes et al. 1989), and consists of at least seven sources aligned along a ridge, similar to OMC-3 in Orion A (Johnstone & Bally 1999; Chini et al. 1997). Relatively more mass exists in the filamentary gas in the latter region. Two of these cores (FIR 4 and FIR 5) are the origins of unipolar molecular outflows, one of which is very highly collimated and very extended (Sanders & Willner 1985; Richer et al. 1992; Chandler & Carlstrom 1996), while the FIR 6 core exhibits a compact outflow (Chandler & Carlstrom 1996) and contains a water maser (Genzel & Downes 1977), a signature of intermediate-mass protostars. The rest of the cores show no sign of star formation activity (Visser et al. 1998). Fukuda & Hanawa (2000) present a numerical simulation of triggered star formation along a filament by the expansion of an H II region and apply their analysis to NGC 2024 in particular. In their picture, compression triggers two cores (i.e., FIR 4 and FIR 5) to collapse, and then at a later time, further collapse is triggered further up and down the filament. This sequence was observed by Chandler & Carlstrom (1996) in their study of outflows from NGC 2024, where the dynamical ages of outflows from FIR 5, FIR 4 and FIR 6 are $1.4 \times 10^4 \text{ yr}$, $2.6 \times 10^3 \text{ yr}$, and 400-3300 yr.

Magnetic fields play a crucial role in the process of star formation, through the magnetic support of molecular clouds, dissipation of angular momentum in accretion disks, and the generation of jets and outflows (see Heiles et al. (1993) and references therein). Polarized thermal emission at submillimeter wavelengths from aligned dust grains traces the direction of the magnetic field structure projected onto the plane of the sky (Hildebrand

1988). Absorption and scattering are usually negligible in the submillimeter. This is in contrast to optical and near infra-red polarimetry, where both of these processes can cause contamination. With the recent development of focal plane bolometer arrays equipped with polarimeters, sensitive imaging polarimetry in the submillimeter is now possible.

Polarimeters functioning at $100\text{ }\mu\text{m}$ (aboard the Kuiper Airborne Observatory), $350\text{ }\mu\text{m}$ (at the Caltech Submillimeter Observatory), and $850\text{ }\mu\text{m}$ (at the James Clerk Maxwell Telescope) have detected polarized emission from dust toward many Galactic molecular clouds. These include the well-studied OMC-1 core in Orion (Schleuning 1998; Schleuning et al. 1997; Coppin et al. 2000; Dotson et al. 2000); Sagittarius A (Aitken et al. 2000); Sagittarius B2 (Dowell et al. 1998) and recently OMC-3 in Orion (Matthews & Wilson (2000, hereafter Paper I); Matthews et al. (2001, hereafter Paper II); Dowell 2001, in preparation). Numerous protostellar and starless cores have also been mapped (i.e., Holland et al. (1996); Ward-Thompson et al. (2000)).

Polarimetry provides information only on the plane-of-sky magnetic field orientation, but no direct information about the magnetic field strength, since the degree of polarization is also dependent on other factors such as grain shape, degree of alignment, and composition. To obtain information about the magnetic field strength requires observation of Zeeman splitting of molecular or atomic spectral lines, which additionally provides information about the direction of the field along the line of sight.

In this paper, we present the first submillimeter polarimetry of the NGC 2071 core and the LBS 23N region. Zeeman observations do not exist toward either of these two clouds. Far-infrared polarimetry at $100\text{ }\mu\text{m}$ (Dotson et al. 2000) and Zeeman splitting observations of OH (Crutcher & Kazès 1983; Kazès & Crutcher 1986; Crutcher et al. 1999) exist for the NGC 2024 ridge of cores. In § 2, we describe the $850\text{ }\mu\text{m}$ observations and the data reduction. The data are presented in § 3 and the polarization patterns are interpreted in § 4. We summarize our results in § 5.

2. Observations and Data Reduction

The observations presented here were obtained on 1998 September 7 and 8 using SCUBA (Submillimeter Common User Bolometer Array) (Holland et al. 1999) at the James Clerk Maxwell Telescope² combined with the SCUBA polarimeter (Greaves et al. 2000, 2001b). The nights were very stable, with $\tau(225\text{GHz})$ ranging from 0.05 to 0.07 during the period of observations. Calibration of the polarizer was performed on 1998 September 5 using the Crab Nebula, for which a percentage polarization $p = 19.3 \pm 4\%$ and position angle $\theta = 155 \pm 5^\circ$ were measured.

Observations were made of two overlapping fields toward NGC 2024, and one field each toward NGC 2071 and LBS 23N. Each polarization cycle consists of 16 integrations at 22.5° rotation intervals in 8 minutes integration time. Six observations (48 minutes integration time) were made toward NGC 2071 and each position toward NGC 2024, and 27 observations (3.6 hours integration time) were made toward LBS 23N.

For each polarization cycle map, the raw SCUBA data were reduced using standard SCUBA software (Holland et al. 1999) to perform nod compensation, flatfielding and extinction corrections. More information on the polarimeter and its data cycle can be found in Greaves et al. (2000). For polarimetry data, extinction is estimated by extrapolation from the current CSO tau value at 225 GHz. Bolometers with anomalously high noise were flagged, and the data were clipped at the 10σ level. Sky noise and instrumental polarization (IP) removal was then performed. The removal of sky noise is, even for basic SCUBA data, a task fraught with danger, but is even more so for polarimetry. The techniques of sky removal are discussed in detail in Paper II; we have taken care to select empty bolometers for sky subtraction.

To first order, the removal of sky effects is achieved by chopping the JCMT secondary during SCUBA observations. Systematic errors can be introduced if significant polarized flux exists at the chop, or reference, positions. Large chop throws

²The JCMT is operated by the Royal Observatory Edinburgh on behalf of the Particle Physics and Astronomy Research Council of the United Kingdom, the Netherlands Organization for Scientific Research, and the National Research Council of Canada.

of $150''$ were used for these observations ($180''$ is the maximum for the JCMT) to try to chop as far off the bright emission as possible. The possible effects of polarized flux in the reference beams (or bolometers used for sky removal) are discussed in Paper II.

Since we have access to large-scale $850\text{ }\mu\text{m}$ scan maps of Orion B north (Mitchell et al. 2001) and south obtained by the Canadian Consortium for Star Formation Studies at the JCMT, comparisons can be made between intensities of candidate bolometers for sky noise subtraction in the on-source position and the fluxes in the corresponding chop positions. For two of our regions, NGC 2024 and NGC 2071, comparison reveals that the differences between these two positions are significant, and that no bolometers on-source were “empty”. The region around LBS 23N, on the other hand, reveals the same flux levels at the chop positions as at the edges of the on-source pointing. Thus, some bolometers at the edges of that map had average intensities of zero. To deal with sky bolometers which do not contain zero flux, the mean value per bolometer removed during sky noise subtraction is added back into the maps of NGC 2024 and NGC 2071, increasing the intensity in each bolometer. The main consequence of this addition is to reduce the polarization percentage, which is inversely proportional to I .

After correcting for source rotation across the array, the Stokes’ parameters were calculated by comparing measurements offset by 45° in wave-plate rotation (90° on the sky). The I , Q , and U maps for each pointing center were averaged, and standard deviations were derived by comparing the individual data sets. The two overlapping fields toward NGC 2024 were then combined into a mosaic; polarization data are uncalibrated, so the data were combined simply by averaging. Since no absolute flux calibrations are done on polarimetry data, the zero points are unknown. This presents problems for creating maps requiring more than one SCUBA field, since one does not know which field contains the best base level to use as reference. We want to obtain the best estimates of uncalibrated flux without giving undue weight to either of our mapped fields. This was done by averaging the baseline levels in the two maps.

The maps were then binned spatially by a factor of 3 (NGC 2071) or 4 (NGC 2024 and LBS 23N)

in both RA and DEC to yield 9 or $12''$ sampling. Selection of “good” polarization vectors is done by filtering out all vectors for which $p < 1\%$ (since the IP values are accurate to just $\pm 0.5\%$) and then filtering by signal-to-noise of polarization percentage, uncertainty of polarization percentage, and the intensity level as appropriate to each field. The thresholding of p ensures that the effects of sidelobe polarization are low (see § 2.1). As further confirmation of the observed polarization patterns, we divided the data sets for each source into two subsets and performed complete reduction on each. The polarization patterns were qualitatively consistent with one another in all cases.

We have truncated our selection of vectors at levels of 2% of the NGC 2071IR peak intensity, 2.5% of the NGC 2024 source peak and 4% of the LBS 23N peak. Paper II illustrates that percentage polarizations and position angles are reliable down to these levels in cases where the reference position’s intensity is approximately 2% of the source peak intensity and the polarization percentage in the reference position is no greater than that of the source field. Thus, in the lowest flux regions, the polarization percentage could be overestimated by up to a factor of two while the polarization position angle is incorrect by $< \pm 10^\circ$. Since JCMT data obtained by chopping off the source record only the difference between these two positions, our data provide no information about the polarized emission at the reference position. However, based on more extensive intensity maps produced by the scan-mapping technique, the chop positions are approximately 1% , 2% and $< 1\%$ of the on-source peaks for NGC 2071IR, NGC 2024, and LBS 23N respectively. These are effectively lower limits to the fractional fluxes relative to the peaks, since scan mapping data may remove the fluxes of very extended features. If there is a uniform background chopped out of the scan maps as well, then the reference position could in fact contain a more significant fraction of the source peak flux.

2.1. Sidelobe Polarization

Even though the sidelobes of the JCMT beam contain less than 1% of the main beam power at $850\text{ }\mu\text{m}$, significant polarization can be measured there because the two incoming planes of polarization experience different optical effects. This

can produce significant *sidelobe polarization*, that can become a source of systematic error especially when mapping extended fields in which the source located in the main beam is fainter than sources elsewhere in the SCUBA field. One can estimate the minimum believable source polarization percentage from the expression:

$$p_{crit} \geq 2 \times p_{sl} \left(\frac{P_{sl}}{P_{mb}} \right) \left(\frac{F_{sl}}{F} \right) \quad (1)$$

where p_{sl} is the IP in the relevant part of the sidelobe, P_{sl}/P_{mb} is the ratio of the sidelobe power to that in the main beam, and F_{sl}/F is the ratio of the mapped source flux in the sidelobe to that in the main beam (Greaves et al. 2001b). Basically, p_{crit} is an estimate of the polarization percentage produced by the sidelobe source alone; hence only polarizations in excess of that value are believable.

For the regions of NGC 2071 and LBS 23N, sidelobe polarization will be minimal, since in both those fields, the field centers were located at the submillimeter peaks. However, in NGC 2024, our northern mapping field was centered roughly on FIR 3, but FIR 5 was at the edge of the SCUBA map, approximately 70" from the center. The ratio of the FIR 5 flux to the central flux is ~ 3.4 . Using a map of Saturn from 31 August 1998, the average power at 70" from the field center is approximately 0.3% of the main beam. The average instrumental polarization is 5.5%. Substitution in equation (1) yields $p_{crit} \geq 0.11\%$. The planetary map was generated with a chop throw of 120", somewhat less than the 150" chop used in NGC 2024. However, using planetary data on Saturn from 11 October 1999 with a 150" chop, we obtain an estimate of $p_{crit} \geq 0.2\%$. Hence, we are confident that our thresholding of polarization percentage at 1% removes all effects of sidelobe polarization in our maps.

3. The Polarization Data

The polarized emission in the submillimeter is thermal emission originating from rapidly spinning non-spherical grains, which are expected to be aligned, on average, perpendicular to the magnetic field. The precise details of the alignment processes are not entirely understood. However, it is well understood that supra-thermally rotating grains align perpendicular to the magnetic field

on very short time-scales. Thus, grain alignment depends critically on the mechanisms by which grains are accelerated to supra-thermal rotational velocities. Radiative torques from short wavelength radiation (Draine & Weingartner 1996) and the well-known Purcell "rocket" mechanism (Purcell 1979) have both been proposed as candidate mechanisms. At present, however, these mechanisms appear insufficient to accelerate grains to the required rotational speeds in regions of high optical depth within molecular clouds (Lazarian et al. 1997). However, the data presented in this paper, as well as recent papers by other authors (Paper II; Dotson et al. (2000); Schleuning (1998)) provide evidence that grain alignment does occur in dense regions of molecular clouds and that the underlying field structure is well-ordered, as demonstrated by the highly structured polarized emission seen in our maps. Johnstone et al. (2001) compare 850 μ m data of NGC 2071 and LBS 23 to CS $J = 2 - 1$ maps by Lada et al. (1991a) and conclude that these clumps of dust emission occur within regions above a column density threshold of $N(H) \sim 10^{22} \text{ cm}^{-2}$, which corresponds to an $A_V > 5$. Thus, the 850 μ m dust emission is associated with extinctions exceeding those at which radiative alignment is expected to be significant. This result poses an important challenge for grain alignment models.

The shapes of grains, their size distribution, their composition, and the details of their alignment mechanisms all strongly affect the ability of grains to produce polarized thermal radiation, and hence influence the resulting polarization patterns. None of these factors are well-constrained, either theoretically or observationally. However, Fiege & Pudritz (2000c) developed a pragmatic approach that combines *all* of the grain and alignment properties for a distribution of grain species into a single parameter $\langle \alpha \rangle$, which can be obtained observationally. This parameterization permits modeling of polarization patterns without detailed knowledge of grain and alignment physics. It was assumed in Fiege & Pudritz (2000c) that all grain species are uniformly mixed with the gas and aligned to the same extent everywhere within the cloud, which implies that $\langle \alpha \rangle$ is constant within any given cloud. However, their model is easily extended to allow systematic variations in grain and alignment properties throughout the cloud,

by simply allowing $\langle \alpha \rangle$ to be a function of either the density, or the distance from the centre of the cloud. We find that allowing $\langle \alpha \rangle$ to vary within a cloud does not typically have a large impact on the geometry of the polarization patterns, although the polarization percentage and the degree of depolarization toward bright sources can vary more substantially. In this sense, our models are quite robust against changes to the underlying grain composition and alignment properties.

If we assume, for now, that $\langle \alpha \rangle$ is constant, then the maximum possible polarization percentage (for the most favourable geometry) with a constant field parallel to the plane of the sky, is given by the formula

$$p_{max} = \frac{\langle \alpha \rangle}{1 - \langle \alpha \rangle / 6} \quad (2)$$

(Fiege & Pudritz 2000c). The maximum polarization percentages for the three regions that we have mapped are 15% for NGC 2071, 13% for NGC 2024, and 22% for LBS 23N. The value for LBS 23N may be anomalously high; the next highest percentage measured is 12.6%. Therefore, 15% is a reasonable maximum value for NGC 2071, with 13% an upper limit for NGC 2024 and LBS 23N. Using 15% as an upper limit on the polarization percentages in these regions, and assuming this is close to the theoretical maximum for a line of sight passing through a magnetic field with ideal geometry, then we find that $\langle \alpha \rangle \approx 0.14$ for all three regions. This estimate is really a lower bound for $\langle \alpha \rangle$ because the observed polarization percentage is reduced by any component of the field lying along the line of sight. Nevertheless, we are encouraged that our estimates of $\langle \alpha \rangle$ do not vary enormously between the three regions, and conclude that $\alpha = 0.14$ is a reasonable global estimate for $\langle \alpha \rangle$ in Orion B. We use this value of $\langle \alpha \rangle$ to generate models of NGC 2024 (see §4.3).

3.1. Polarization Patterns

3.1.1. NGC 2071

In Figure 1, we present the 850 μm polarization vectors of NGC 2071 IR, superimposed on a false color image of the 850 μm dust emission (from Mitchell et al. (2001)). The inset shows a “blow-up” of the central region in order to show the weak polarization features better. The data

are also presented in Table 1 of Appendix A.

Toward the region of strongest emission (the IR cluster), the percentage polarization is quite weak, typically less than 2%. However, polarization as strong as 15% is measured toward fainter parts of this region. The polarization pattern is highly symmetric, including the curvature of the vector orientation around the peak to the northeast and southwest. Over the entire core region, the vectors exhibit a mean orientation of 20° east of north. Based on low-flow velocities of HCO^+ maps of the dominant outflow in the region, Girart et al. (1999) estimate its overall position angle to be $\approx 40^\circ$ (east of north). Figure 1 shows this outflow orientation schematically. Closer to the emission peak, the dominant position angle is $\sim 30^\circ$, which is within 10° of the outflow’s orientation. The outflow is thus well-aligned with the polarization vectors.

Qualitatively, the polarization pattern is similar to that of OMC-1, which was interpreted as evidence for an hourglass magnetic field geometry in that region (Schleuning 1998). In this picture, the magnetic field is pinched toward the central source due to flux freezing with the infalling gas. However, we do not observe the same sort of flattening of the NGC 2071 core that is evident in the 350 μm flux map of OMC-1 (Schleuning 1998). The NGC 2071 core maintains a circular shape even far from the peak, with no suggestion of oblateness or prolateness (see Figure 1).

3.1.2. LBS 23N

Figure 2 shows the dust polarization of the LBS 23N source and its surrounding region (the data are also presented in Table 2 of Appendix A). A string of cores is surrounded by a faint filamentary background of dust emission. The dominant orientation of the polarization pattern is north-south, except at the southern boundary, where the vectors lie almost east-west. The strongest polarization (22%) is seen in the east and west limbs of the “filament”.

It is intriguing that the vectors abruptly change direction by 90° near the southern-most boundary of our polarization map to become aligned east-west. The 850 μm continuum map of Mitchell et al. (2001) shows that the underlying dust structure widens south of our polarization map to a fil-

amentary segment oriented roughly east-west (see Figure 2). A similar shift of polarization orientation has been observed in the southern part of the OMC-3 filament in Orion A, where the filament's projected width on the plane of the sky appears to increase (Papers I and II). We discuss three possible interpretations of our data in § 4.2. Polarimetry in the southern region of LBS 23 will help us in our modeling effort to understand the structure of the magnetic field in this region. However, the faintness of the LBS 23 filament will make obtaining the necessary data more difficult than in OMC-3.

3.1.3. NGC 2024

The polarization pattern of the molecular ridge of NGC 2024 is shown in Figure 3, superimposed on a false color image of the 850 μm dust emission.³ The data are presented in Table 3 of Appendix A. Seven continuum sources (FIR 1-7) have been identified along the ridge (Mezger et al. 1988, 1992). In the north (FIR 1-4), the vectors along the peaks are weak and parallel to the ridge. The southern sources (FIR 5-7) have very weak polarization toward the brightest cores and are significantly depolarized. To the east and west, the polarization becomes quite intense (up to 10%), and a change in vector orientation of approximately 90° is observed from west to east.

Linear polarization at 100 μm has been observed previously toward this region with the Kuiper Airborne Observatory (Hildebrand et al. 1995; Dotson et al. 2000). These data are centered on the FIR 5 core and cover the same area as our map. Figure 4 shows our polarization data and those of Dotson et al. (2000) at 100 μm plotted over contours of the 850 μm total emission. The 100 μm data are more sparsely sampled than the SCUBA data (owing to the 35'' beam), but the two patterns are remarkably consistent. The vectors trace the same V-shaped pattern seen at 850 μm , although the finer sampling by SCUBA makes the pattern much easier to see. The chop throw of the KAO observations was 10.5', over four times greater than that used for our data set. The fact that the polarization patterns are very consistent suggests that the position angle at least has not

been strongly affected by any systematic effects due to chopping. The maximum polarization percentage measured at 100 μm is $5.86^{+0.01}_{-1.00}\%$, while the minimum vector has a polarization percentage of $0.36^{+0.06}_{-0.07}\%$ and a position angle of $164.9 \pm 5.2^\circ$ (east of north), where the uncertainties are absolute upper limits. At roughly the same position, the 850 μm polarization is $1.63 \pm 0.15\%$ at an angle of $-20.7 \pm 2.7^\circ$ (equivalent to $159.3 \pm 2.7^\circ$). This is a relatively low polarization percentage at 850 μm , and the position angles of the vectors agree within measurement uncertainties. At 850 μm , the maximum and minimum polarization percentages are $13.41 \pm 1.13\%$ and $1.02 \pm 0.09\%$. Where the northern and southern parts of the filaments meet (i.e., between FIR 4 and 5), there is significant depolarization regardless of the low flux level. Depolarization in the filamentary material away from the cores is also observed between cores in OMC-3 in Orion A (see Paper II).

There is no obvious correspondence between the polarization position angles and the directions of outflows in the region. The strongest outflow is unipolar and extends from FIR 5 to the southeast (Richer, Hills & Padman 1992). Greaves, Holland & Ward-Thompson (2001) have measured polarized spectral line emission from the CO $J = 2 - 1$ line utilizing the Goldreich-Kylafis effect (Goldreich & Kylafis 1981) in the outflow of FIR 5. The polarization vectors measured in the outflow are plotted on Figure 3, along with the orientation of the outflow itself. For large CO optical depths, line polarization is parallel to the field, unless the field is at a large angle to the velocity gradient (Kylafis 1983). Therefore, Greaves et al. (2001a) conclude that the magnetic field associated with the outflowing gas is aligned with the outflow itself. If the large scale field in the region maintains the same orientations, we would expect the continuum polarization vectors to lie perpendicular to the outflow. But the continuum vectors do not exhibit this behavior. Nor does their orientation appear to be influenced by their proximity to the outflow. The dust polarization data do not exhibit an obvious correlation with either the outflow or the line polarization data which traces its magnetic field. Thus, we conclude that a complex field geometry threads this region.

³JCMT data taken by Canadian Consortium for Star-Formation Studies, as yet unpublished.

3.2. Depolarization toward High Intensities

As observed in many other regions, a declining polarization percentage is detected toward regions of increasing intensity in each of our fields. Figure 5 shows the percentage polarization as a function of unpolarized I for each region. The depolarization effect is clearly a global feature in our maps and is not limited to a single region or core. The slopes of Figure 5 range from -0.5 to -0.9 , but the trend of declining polarization percentage is clear. The same trend was measured in the OMC-3 region of Orion A (see Paper II). It is possible for a “polarization hole” to result from a systematic error produced by chopping to remove background sky during observing. However, Paper II shows that depolarizations as steep as those measured in Orion B (i.e., slopes of $\log I$ versus $\log p < -0.55$) cannot be produced by the effects of chopping alone, particularly at high values of I , even for the case where the flux at the reference position is 25% that of the source peak and the reference polarization percentage is twice that of the source. Therefore, there must be a physical cause for this effect.

The issue of depolarization in dense regions is particularly interesting as a test of alignment mechanisms. Grain alignment theories at present cannot explain why grains are so well aligned in regions of high optical depth within molecular clouds. For example, the Purcell mechanism (Purcell 1979) and its variations are not likely to work in these regions, where atomic hydrogen is almost completely absent (Lazarian et al. 1997). The radiative alignment mechanism (Draine & Weinberg 1996), which aligns grains efficiently in the ISM, is unlikely to work in dense molecular regions, where short wavelength starlight (needed to spin up and align grains) is extinguished. Appealing to embedded sources to provide the necessary radiation is not likely to help, since this would predict the best alignment to be associated with the dense regions around evolved protostars, while the opposite is observed. Thus, our observations pose an interesting and extremely important challenge for grain alignment theory.

We consider 3 possible explanations for the “polarization hole” effect. First of all, it is possible that the depolarization in our maps are the result

of grains in the central regions of highest density that are either poorly aligned, or intrinsically poor polarizers (Weintraub, Goodman & Akeson 2000; Goodman et al. 1995). In such a case, all dust grains through the cloud contribute to the continuum intensity, but only the fraction that are aligned contribute to the polarized flux given by the Stokes’ vectors Q and U . Therefore, toward regions of high intensity, the ratio of polarized to total intensities is systematically reduced. Alternatively, Fiege & Pudritz (2000c) proposed that the depolarization could result from the large scale field structure itself, since helically twisted fields result in depolarization as a result of oppositely signed contributions to the Stokes’ vectors from the poloidal and toroidal field components. This field geometry has been used to model the OMC-3 part of Orion A’s Integral-shaped Filament (Paper II), and we show a similar model for NGC 2024 in § 4.3.1 below. A third possibility is that a disordered, or tangled, field exists on scales smaller than our beam, and the field averages to zero in the JCMT’s 14'' beam. It is possible that more than one of these effects could be contributing to the depolarization observed in our maps.

Interestingly, NGC 2071 does not exhibit a polarization hole coincident with the peak of the dust emission; instead, two polarization holes are detected, offset to the northeast and southwest of the dust emission peak. These polarization holes are not due to bad bolometers or low signal-to-noise. The degree of polarization in those locations is less than 1% and is thus considered negligible at these positions. In NGC 2024, depolarization is so significant in the case of FIR 5-7 that polarization is negligible across those cores. In LBS 23N, depolarization can be seen in Figure 2 toward the brightest core, OriBN 59 (see Mitchell et al. (2001)). It is difficult to sample the depolarization in the fainter sources of Figure 2 because they are unresolved, but OriBN 58 does show significant depolarization. Our mapping does not extend to the OriBN 60 core, and further data toward LBS 23 (south) will be needed to determine whether or not the observed depolarization extends to this region.

4. Interpreting Polarization Patterns

Polarization vectors in the submillimeter are perpendicular to the direction of the magnetic

field component in the plane of the sky, appropriately averaged along the line of sight through the cloud. However, it is generally insufficient to infer the field structure by simply rotating the polarization vectors by 90°, since this procedure implicitly assumes that the direction of the plane of sky component of the magnetic field is constant. Magnetic fields in molecular clouds are almost certainly curved in three dimensions, which violates this condition for all but the simplest geometries. A simple example serves to illustrate that this technique fails. Fiege & Pudritz (2000c) recently calculated the polarized emission from their models of filamentary clouds threaded by helical magnetic fields (Fiege & Pudritz 2000a). This was done by numerically integrating the contributions to the Stokes' vectors along lines of sight through the filament. They demonstrated that the polarization is always parallel or perpendicular to the symmetry axis of the filaments in the plane of the sky, (sometimes with sudden 90° flips in orientation at some radial distance). Now, if we try to interpret the resulting polarization maps by simply rotating the polarization vectors derived from their models, we discover that this approach does not resemble the input helical field geometry. A more sophisticated approach is generally required to compare candidate models, threaded by non-trivial 3-dimensional magnetic fields, with the data. This must involve direct modeling of polarization patterns.

It is important to note that interpretations of polarization data are somewhat degenerate. By varying the magnetic field geometry and the polarization efficiency of the grains, it is often possible to produce a qualitatively similar polarization map from more than one field geometry. An example of this difficulty is given in § 4.3, where we present two alternate models of our NGC 2024 polarization map. It is generally impossible to *uniquely* determine the 3-dimensional structure of the magnetic field from polarization data alone. Nevertheless, polarization maps can be used to provide strong constraints on models of magnetized clouds, filaments, and cores as follows. 1) On the basis of polarization data alone, it is often possible to rule out models that are inconsistent with the data when viewed from all possible orientations. For example, in Paper II, we were able to rule out all models of the Integral-shaped Fil-

ament in Orion A that are threaded by a purely poloidal field. 2) All existing magnetohydrostatic models of clouds, filaments, and cores are axisymmetric. The assumption of axisymmetry reduces the set of models to be compared with the data which limits the allowed configurations. We find that much of the polarization degeneracy is lifted when only axisymmetric models, or perturbations of axisymmetric models (see § 4.3.1), are considered. We also find that certain field structures produce identifiable, although sometimes surprising, “signatures” in the polarization data, which can be used as a guide toward developing detailed models. 3) There are few regions where both polarization data and Zeeman data exist. Zeeman data can be combined with the polarimetry to construct a more nearly unique model than could be determined by polarimetry alone, since Zeeman observations measure the line of sight component of the magnetic field. However, one must be extremely careful because Zeeman measurements and submillimeter polarimetry usually trace different components of the gas. An interpretation that combines Zeeman data and polarimetry implicitly assumes that the field is related in these components. We combine polarization and Zeeman data in § 4.3.2, where we model the NGC 2024 as a shell swept up by an H II region around a dense ridge.

An alternative approach is to compare the data with polarization maps predicted from simulations. The cores arising in simulations are not generally in equilibrium, and the field simulations are not generally axisymmetric. This technique has the potential to provide useful insight into the general statistical behavior of polarization maps for ensembles of objects. Padoan et al. (2001) have applied the polarization modeling technique developed by Fiege & Pudritz (2000d) to simulations of MHD turbulence. They find that the relationship between polarization percentage and submillimeter intensity is a robust statistic, which can be used to constrain models of grain alignment. A limitation of turbulence simulations is that they cannot be easily used to model specific objects, which is the focus of this paper.

4.1. NGC 2071

NGC 2071 is a massive core that has no associated filamentary structure. Nevertheless, there are some strong similarities between this core and

OMC-1, even though the latter is associated with the massive Integral-shaped Filament of Orion A. There are no Zeeman data toward NGC 2071, so the polarization data alone constrain the field geometry. The polarization map is similar to the 100 μm polarization map of OMC-1 made by Schleuning (1998). In that region, the polarization data are interpreted as indicating an “hourglass” magnetic field, which developed as the core contracted perpendicular to field lines. The contraction is centered on the infra-red source known as KL. However, there is an important difference between Figure 1 and Schleuning’s 100 and 350 μm maps. The OMC-1 core exhibits a flattened structure, whose long axis (in projection) is parallel to the mean direction of the polarization vectors. This is precisely what one would expect for an oblate core threaded by an hourglass field (Mouschovias 1976; Tomisaka, Ikeuchi, & Nakamura 1988). However, the NGC 2071 core is not flattened at all. There is no evidence of elongation either parallel or perpendicular to the outflow in our data (see Figure 1) or the 50 and 100 μm observations of Butner et al. (1990).

The direction of the most powerful outflow of NGC 2071, thought to originate from the source IRS 3, is shown in Figure 1. It is aligned at a position angle of 40° (east of north). The mean polarization position angle in our data set is $\sim 22^\circ$, with a dispersion about the mean of 32°. In the subset of vectors toward the peak, the mean position angle is 34° with a standard deviation about the mean of 33°. The vectors are generally consistent with the direction of the outflow.

Houde et al. (2001) have recently used a new technique, which compares the line profiles of the coexisting neutral (HCN) and ionic (HCO^+) species, to show that the outflow’s magnetic field and its direction are well-aligned in NGC 2071. However, our polarization data suggest a magnetic field that is either orthogonal to the outflow direction, or strongly toroidal about an axis parallel to the outflow. In either case, the magnetic field in the core does not appear to coincide with the field in the outflow. The first possibility would be difficult to reconcile with theory, unless the magnetic field at the small scales where the outflow originates is unrelated to the large scale field threading the core. It would be especially problematic for models of protostellar formation that favor col-

lapse along field lines, resulting in outflows aligned with the field of the core. This possibility would substantially diminish the role of magnetic fields in protostellar collapse. The latter possibility is more intriguing because it could be reconciled with a class of self-similar outflow models proposed by Fiege & Henriksen (1996) and elaborated on by Lery et al. (1999). These models permit a magnetic field which is primarily toroidal in the dense, partially pressure supported, gas near the equatorial plane, even far from the central star. The topology of the field is quadrupolar in the poloidal plane, so that the field is almost radial near the symmetry axis defined by the outflow direction and parallel to the outflow.

Motte et al. (2001) have compared the SCUBA 850 μm emission from NGC 2071 to pre-existing maps of CO $J = 3 - 2$ and $\text{HCO}^+ J = 4 - 3$ (Chernin & Masson 1992) and find that up to half the emission in the 850 μm bandpass could be originating in the outflow’s line emission. This could affect the interpretations given above. Motte et al. (2001) estimate that $> 20\%$ of the continuum emission at 850 μm could arise from the CO $J = 3 - 2$ line. According to theory, in the case of high density gas, the linear polarization produced in spectral lines should be parallel to the magnetic field. Even if the magnetic fields giving rise to the dust and line polarizations were perfectly aligned, they would contribute orthogonal vectors to the net polarization. Thus, the usual interpretation of submillimeter continuum polarization as being orthogonal to the plane-of-sky component of the magnetic field could be incorrect in regions where the CO emission is strong enough to dominate the continuum flux from dust. If our polarization data were dominated by line emission, then the inferred field direction would align to within 10° of the CO outflow. However, where the CO emission is optically thick, the maximum polarization contributed by the outflow is on the order of 1%, as is the case for CO $J = 3 - 2$ emission from the outflow of FIR 5 in NGC 2024 (Greaves et al. 2001a). Therefore, when dust polarizations exceed 1%, they are unlikely to be dominated by CO line contamination (J. Greaves, private communication). Therefore, we conclude that the strong polarizations measured toward this core are dominated by dust emission and hence do not infer a magnetic field aligned with the outflow direction.

Finally, we note that the orientation of the outflow relative to the core's magnetic field may turn out to be inconsequential. NGC 2071 is a massive core forming many stars. This is very different from the case of low mass cores forming isolated stars, to which most of the existing theory applies. Within several star-forming regions, multiple outflows of various orientations are observed, i.e., OMC-2/3 in Orion A (Aso et al. 2000; Yu et al. 2000). If the collapse of massive cores is really dominated by the mean magnetic field, then one might expect a rough alignment between all outflows originating from the same core. Since this is not observed in NGC 2071 (Eislöffel 2000), it is unclear how relevant the large-scale field is in determining the orientation of outflows.

4.1.1. An Estimate of Magnetic Field Strength

Chandrasekhar & Fermi (1953a) demonstrated that when a mean field direction can be defined, the magnetic field strength can be derived using the dispersion in polarization angles, σ_θ , the dispersion in velocity along the line of sight, $\sigma_{v_{los}}$, and the mean density, ρ , in the region local to the polarization and velocity data. In cases of complex, ordered field geometries, it is no easy task to assign a mean field direction based on polarization data (see §§4.2 and 4.3 below). However, in NGC 2071, we can apply the method of Chandrasekhar & Fermi (1953a) assuming that the field threading the core is relatively straight. The mean field strength, $\langle B \rangle$, is given by

$$\langle B \rangle = \left[4\pi\rho \frac{(\sigma_{v_{los}})^2}{(\sigma_\theta)^2} \right]^{1/2}. \quad (3)$$

The NGC 2071 core was mapped in NH₃ (1,1) emission at high velocity resolution by Takano et al. (1986). The ammonia emission extends over 2' from the dust peak location and shows more elongation than the dust map. (Takano et al. 1986) identified three components in the line profiles from across the core. The narrowest feature is described as a “spike” in the profile and is seen over the entire mapped area. This emission is attributed to the core itself (as opposed to any outflowing gas). The FWHM of this component is estimated to be 1 km s⁻¹, which corresponds to a dispersion of approximately 0.5 km s⁻¹. Ammonia traces relatively high density gas ($n(H_2) \geq 10^4$

cm⁻³), so we use 10⁴ cm⁻³ as an estimate of the mean density across the core. As discussed above, the dispersion in polarization angles at 850 μ m is 33°, which corresponds to 0.58 radians. Substitution of these values into equation (3) yields $\langle B \rangle \approx 56 \mu$ G which is consistent with what would be expected within a dense core.

Heitsch et al. (2001) propose an amendment to the Chandrasekhar and Fermi model which yields an estimate of the rms field strength. In the case of equipartition between the magnetic and kinetic energies, the total magnetic energy is given by

$$\langle B^2 \rangle = 4\pi\rho \frac{(\sigma_{v_{los}})^2}{(\sigma_\theta)^2} [1 + (3\sigma_\theta^2)] \quad (4)$$

which gives similar results to equation (3) when the field is highly ordered. For NGC 2071, we find that the ratio of the total magnetic energy, $\langle B^2 \rangle$, to the mean field energy, $\langle B \rangle^2$, is 2. Using the values for NGC 2071 above, the rms field is estimated to be 78 μ G, a factor of 1.4 times greater than the mean field.

Crutcher (1999) compared the densities within star-forming clouds with the line-of-sight field strengths measured using the Zeeman effect on molecular lines. Based on his compilation of all existing data, he concluded there was no substantial evidence against equipartition in star-forming clouds. The line-of-sight field strength, B_{los} , can be extrapolated from the mean field strength based on a statistical average over all potential inclinations of the field to the line of sight. We estimate B_{los} to be roughly the mean field divided by 2, or 28 μ G. Comparing this field strength to the density within the NGC 2071 core of 10⁴ cm⁻³ using Table 1 of Crutcher (1999), it is clear that this value is comparable to measurements of the Barnard 1 dark cloud core, but substantially less than the more massive M17 cloud.

Based on this comparison, we conclude that, while the Chandrasekhar-Fermi method does give a value of mean field strength consistent with those measured directly using Zeeman splitting, it also predicts that approximately half the magnetic energy does not reside in the mean field component. These results are not surprising given the fact that an ordered pattern is observed in the polarization data which is not straight. Thus, we should not be too quick to attribute the rest of the magnetic energy to turbulence. However, direct measurement

of Zeeman splitting of OH lines at several positions in NGC 2071 would provide a further test on the validity of a simple, mean field geometry within this cloud.

4.2. LBS 23N

The polarization structure of the LBS 23N region is somewhat less orderly than that of either NGC 2071 or NGC 2024, and there are no Zeeman data toward this region. However, there remains sufficient structure in the polarization map to warrant some comparison to filamentary models. The LBS 23N region is a linear string of roughly equally spaced condensations, which might be the result of fragmentation due to gravitational instabilities (see Chandrasekhar & Fermi (1953b), Nakamura, Hanawa, & Nakano (1993) and Fiege & Pudritz (2000b) for a discussion of gravitational instabilities in magnetized filaments). The overall orientation of the polarization vectors is along the filament, with some degree of scatter in position angle. The mean position angle in the 70 vectors is 8.7° with a standard deviation of 5.0° .

We offer three possible explanations for such a pattern. The first possibility is that the original filament is threaded by a magnetic field transverse to the symmetry axis. This magnetic field geometry would reproduce the orientation of the majority of the polarization vectors. However, it is not easy to understand how such a field geometry could be associated with a filament or linear string of cores collapsed in three dimensions, since a transverse field would more likely be associated with a sheet-like distribution of material. This geometry also cannot readily explain the 90° flip seen in the polarization vectors toward the southern end of the filament.

Alternatively, Fiege & Pudritz (2000c) proposed that such a pattern could be explained as the result of a helical field dominated by the toroidal field component (Type 1, according to their classification) as observed in the OMC-3 filament of Orion A. Helical field geometry can create polarization patterns where vectors flip by 90° at the interface between poloidally and toroidally dominated regions, which could occur if the field threading the southern part of the filament is less tightly wound than in the north. Such a flip is suggested by our data at the southern end of the polarimetry map. We note that these data pro-

vide only sparse coverage of this region and are the lowest signal-to-noise data of all three regions. Modeling of this region will require observations of the southern part of the filament.

Finally, Paper II presents a model for two crossed filaments, unconnected but overlapping in projection on the plane of the sky. In such a case, the vectors in the overlap region can be dominated by one of the two filaments. The east-west filamentary structure is identified in Figure 2. As for OMC-3, this scenario can be tested by more extensive mapping into LBS 23 south.

4.3. NGC 2024

The overall appearance of NGC 2024's submillimeter emission is that of a short filament, which is broken into three main condensations. The polarization vectors show a complicated but extremely well-ordered pattern throughout the region. An interesting feature of the map is a rather abrupt change in orientation across the central ridge of the filament. This feature cannot be reconciled easily with a purely poloidal field along the filament axis, since that geometry would produce polarization vectors perpendicular to the axis, irrespective of the inclination of the filament. Fiege & Pudritz (2000c) found that polarization vectors can flip by 90° across the central axis of a filament threaded by a helical field, when the filament is inclined at an angle relative to the plane of the sky. However, the polarization vectors in their model are always aligned either parallel to or perpendicular to the filament. This is not the case in our map, where the vectors form a "V" like pattern, with the apex located on the central ridge of the filament. However, we show below that a simple extension to their model can account for the qualitative features of this map.

The interpretation of the polarization pattern is constrained by measurements of the line-of-sight magnetic field component, B_{los} (sometimes denoted B_{\parallel}). Crutcher et al. (1999), using Zeeman splitting of OH absorption lines, detected a peak in B_{los} of almost $100 \mu\text{G}$ at a position west of FIR 4. The field strength declines smoothly from this southwestern position in their map to the northeast, where it drops to zero (cf. their figure 3). OH samples gas densities of approximately 10^4 cm^{-3} , which are substantially lower than the volume densities estimated along the

NGC 2024 molecular ridge. The extended filamentary structure in which the cores are embedded have $\langle n_H \rangle \approx 5 \times 10^6 \text{ cm}^{-3}$, while the cores themselves have $\langle n_H \rangle \approx 2 \times 10^8 \text{ cm}^{-3}$ (Mezger et al. 1992). Thus, it is not certain that the field being traced by the Zeeman data threads the same dense gas whose magnetic field is traced by our polarization measurements. However, the fact that the positions of low polarization percentage in both 100 μm and 850 μm correspond closely with the maximum in line-of-sight field could support a correlation in the fields traced by the two techniques, since low polarizations could indicate a region where B_{los} is dominant. Conversely, the low polarization could be a produced by variations in alignment or grain properties and thus be unrelated to B_{los} . Keeping this uncertainty in mind, we offer two theoretical models for this pattern.

Schulz et al. (1991) measured NH₃ and CS gas toward NGC 2024 and found distributions of dense gas that closely mirrored the pattern of dust condensations. This supported later conclusions that the dense ridge is located on the far-side of the H II region (Chandler & Carlstrom 1996; Crutcher et al. 1999), as originally schematically illustrated by Barnes et al. (1989). We illustrate the most likely configuration in Figure 6. In order for OH to be observed in absorption, there must be a source of background continuum emission. Thus, either the OH Zeeman data trace the field in the foreground dust lanes (with the observable H II region as the continuum source) or the OH absorption is occurring in the denser molecular cloud, thus requiring a second source of continuum emission behind the ridge. For instance, the H II region could have penetrated to different depths of the cloud due to density variations. The latter scenario is favored by Crutcher et al. (1999) with the ridge located on the far side of the H II region.

In the first case, the Zeeman splitting OH absorption data may be sampling an envelope of gas either in the foreground of the H II region itself, or simply at the boundary between the H II region and the very dense molecular cloud behind it, regardless of the location of the dense ridge. In this case, the Zeeman data are unrelated to the polarization data and would not provide a constraint. In the second case, we assume that although the OH data sample a less dense region of gas, the measurements are sampling the same field geome-

try in both regions.

4.3.1. A Helical Field Model

Perfectly straight, infinite filaments are an idealization, which may need to be relaxed somewhat when comparing models with real data. Figure 7 shows a finite segment of a filament model from Fiege & Pudritz (2000a), which we have “bent” into a circular arc using a simple mathematical transformation that maps planes parallel to the axis of the filament into concentric cylinders of some specified mean radius of curvature, orthogonal to the filament axis. The density and magnetic field are transformed self-consistently, using the Lagrangian formulation of the MHD induction equation and the equation of mass conservation (see Parker for example):

$$\frac{\mathbf{B}}{\rho} = \mathbf{J} \frac{\mathbf{B}_0}{\rho_0} \quad (5)$$

$$\rho = \frac{\rho_0}{|\mathbf{J}|}, \quad (6)$$

where \mathbf{J} is the Jacobian of the coordinate transformation and $|\mathbf{J}|$ is its determinant. We will thoroughly discuss the details of our modeling technique in a future paper.

The polarization structure of the theoretical map reproduces most of the qualitative features of Figure 3. On the other hand, models that are threaded by purely poloidal fields do not agree with the polarization data. Note that the model shown is a preliminary result and should not be regarded as our final, best fit to the data. Nevertheless, we have provided the exact parameters of this model in the caption of Figure 7.

It is interesting that a bend in the filament is required to reproduce the polarization pattern shown in Figure 3. If the filament is bent so that the source FIR 5 is closest to the expanding ionization front of the H II region, then this could explain why it is the most evolved source along the ridge. The outflow from this source is the most powerful in the region (Richer et al. 1992), while evidence for less evolved outflows can be found in the sources FIR 4 and FIR 6 (Chandler & Carlstrom 1996).

4.3.2. Expansion of the H II Region around A Dense Filament

The expected Zeeman pattern from a helical field is a reversal in orientation of B_{los} across the symmetry axis of a filament. If the field threading the filament is related to the field in the lower density gas, then the helical field interpretation would not be consistent with the observations of Crutcher et al. (1999) toward the northern portion of the NGC 2024 dense ridge. In order to reconcile the Zeeman and polarization data, we suggest that the magnetic field has been distorted from its original structure by the expansion of the H II region, as shown in the schematic diagram of Figure 8. The field may be pushed out on the surface of the ionization front, but will bend around the dense, filamentary system of cores comprising the NGC 2024 region.

The asymmetric Zeeman data requires one of the following geometries: either the ionizing source is in front of and to the west of the dense ridge; or the density of the molecular cloud itself must increase to the east, thereby inhibiting the expansion of the H II region on that side (Barnes et al. 1989). The contours of Figure 4 show that the dust extends further to the east of the ridge than to the west. If the source of the ionization front is to the west of the molecular ridge, then the vectors seen from our line of sight will stretch across the front of the ridge and to the east nearly in the plane of the sky (i.e., the B_{los} component is zero). To the west of the molecular ridge, such a source would produce an ionization front which would be bending around the ridge, with components B_{los} and B_{\perp} both non-zero.

However, there is substantial evidence that the dense cores and high density gas lie behind the H II region, as shown in Figure 6. Although Barnes et al. (1989) calculated the ionizing radiation detected in the nebula to require the IRS 3 source to be an O9 (or earlier) star, they conclude this to be unlikely unless the extinction toward IRS 3 is 4.1 mag in K , a factor of 2 greater than the average extinction derived toward that star. Instead, they suggest that an ensemble of B stars must have formed the H II region. If each star has formed a bubble of ionized radiation around it, as IRS 2 has produced the Eastern Loop (see Figure 6), then the cumulative effect could produce the

H II region.

In order for this picture to be physically reasonable, the ionization front must be interacting with the molecular ridge. Gaume et al. (1992) detected 1.3 cm emission at 3'' resolution located at south of FIR 4 (their NH₃ 4) and north of FIR 5 (their NH₃ 5). North of the FIR 5 source, the 1.3 cm emission arises from a dense, ionized interface between the molecular cloud (and ridge of cores) and the H II region. Ionized emission near FIR 4 has a compact component associated with the dense ridge. Additionally, higher NH₃ temperatures, larger line widths and smaller abundances suggest that the FIR 4 and FIR 5 sources are nearest the ionization front of the H II region. Schulz et al. (1991) show that ionized gas in fact fills the bay in the molecular bar surrounding IRS 3 (see their figure 7), and that the ridge is effectively separated into two subregions by the ionization front of the H II region. We proceed on the basis that the ridge existed prior to the formation of the H II region.

The polarization model shown in Figure 9 is based on the idea that the magnetic field has been swept up in a shell during the expansion of the H II region and stretched over the surface of the dense filamentary system of cores embedded in the wall of the molecular cloud. The stretching of the field in this scenario would tend to make the field quite uniform by the time the shell reached the system of cores. The structure of the magnetic field is idealized as follows. We assume that the field is swept into a sheet with a Gaussian planar distribution of the form

$$\rho = \rho_c e^{-\frac{(y_0 - y_c)^2}{\delta y^2}} \quad (7)$$

$$B_0 = B_{x0} e^{-\frac{(y_0 - y_c)^2}{\delta y^2}} \hat{x} + B_{z0} e^{-\frac{(y_0 - y_c)^2}{\delta y^2}} \hat{z} \quad (8)$$

when it first encounters the embedded filament, where \hat{y} is along the line of sight, y_c is the offset of the field's center from the filament axis, δy is the width of the field region and B_{x0} and B_{z0} are respectively the maximum, central values of the \hat{x} and \hat{z} field components. The magnetic field threading the shell is generally not aligned with respect to the filament axis, which is oriented in the \hat{z} direction. The filament is assumed to be an unmagnetized, Ostriker (1964) filament, which we have truncated at a radius of $10^C r_0$, where r_0 is the radial scale of the filament given in Fiege &

Pudritz (2000a). This radial scale basically defines the radius where the inner, nearly flat density profile begins to steepen toward the r^{-4} profile that the density obeys at $r \gg r_0$.

We wrap the field threading the shell around the filament by applying a coordinate transformation of the form

$$x = x_0, \quad y = y_0 + r_0(x/w)^2, \quad z = z_0 \quad (9)$$

to the planar field giving by equation (8). The front of the shell is defined by the surface $y_0 = -10^C r_0$, so that it just touches the filament. This transforms the originally planar sheet into a parabolic shell, wrapped around the filament, which is centered on the origin. The magnetic field and density are self-consistently distorted using the Lagrangian forms of the MHD induction equation and the equation of mass conservation, as given by equation 6. The determinant $|\mathbf{J}|$ of the transformation is unity, so that the density is unchanged.

The Zeeman data of Crutcher et al. (1999) suggest that the magnetic field is approximately parallel to the surface of the molecular cloud east of the filament, and strongly bent into the line of sight on the west. This is also supported by Barnes et al. (1989), who suggest that the molecular cloud may be denser east of the ridge than to the west, since the field would be swept further back on the side of lower density. Thus we rotate our field configuration by 20° counter-clockwise (looking toward the origin from the \hat{z} axis) to mimic this asymmetry. The inclination angle that best reproduces the observed polarization map is 60° into the plane of the sky. We apply a final rotation of -15° in the plane of the sky to better agree with the observed orientation of the filament. The resultant polarization pattern is shown in Figure 9. This figure also shows a map of the density-weighted average of the line of sight component of the magnetic field (arbitrary units) for comparison with the Zeeman data.

This model is in better agreement with the Zeeman data for NGC 2024 than the helical field model given in § 4.3.1. However, our magnetized shell model has several shortcomings. The best-fitting polarization pattern that can be obtained from this type of model, with the Zeeman data regarded as a constraint, is of noticeably poorer agreement than the helical field model. The shell

model reproduces the general features of the map, but the helical field model does a better job accounting for the detailed structure. The shell model also predicts a dense ridge of emission on the west side of the filament, where the parabolic shell plunges into the plane of the sky. It is noteworthy that the filament in this model is unmagnetized, and therefore does not contribute to the polarized flux. Hence, it is necessary to put a considerable amount of mass into the shell, so that the polarization percentage, defined as the polarized flux divided by the total intensity, is sufficiently high across the filament to account for the observations. The central density of the shell is 11.4% of the central density of the filament, and the shell's thickness is $10^C/3$. A side-effect of this dense shell is that the emission away from the filament is non-negligible. Both the polarization and the intensity in Figure 9 are clipped at 5% of their respective maximum values. Nevertheless, polarized emission above these levels is found in the background, in contrast to the helical field model, where this clipping procedure eliminates the flux away from the filament.

The depolarization observed in NGC 2024 is easily understood in this model. The filament itself does not contribute to the polarized flux, since it is unmagnetized. Instead, a uniformly polarized foreground sheet produces the polarization. Where the total intensity is high (i.e., along the filament), the polarization percentage declines, as we observe.

A limitation of this model is that the filament is unmagnetized, and therefore obeys the r^{-4} density profile predicted by Ostriker (1964). This density gradient is known to be too steep to account for the observations in other filaments (Alves et al. (1998); Lada et al. (1999); Johnstone & Bally (1999)). A magnetic field threading the filament could be included in this model, in principle, but this would make it substantially more complex.

A third type of model may also be worth considering. We have assumed in the above model that a shell swept up by the H II region wrapped around a dense filament, pre-existing in the cloud behind the H II region. One could imagine an alternate scenario involving the filament fragmenting out of the shell. The fastest growing unstable modes of fragmentation of a magnetized sheet result in filaments oriented either parallel or perpendicular to

the magnetic field, depending on the thickness of the shell (Nagai et al. 1998). In either case, the geometry of the field probably could not account for the complex structure seen in our polarization map. We also note that a fragmenting shell would most likely produce more than one filament, and no others are observed in the vicinity of NGC 2024.

4.4. Further Observational Tests of the Helical Model

Although quantitative comparisons of the filamentary helically-threaded models to 850 μm data (and where applicable, Zeeman data) will constrain which model can reliably reproduce our observations, different observation tests will eventually be possible. For example, observations a) on larger spatial scales, b) over a range of wavelengths, or c) at higher resolutions will each test the helical field models.

If filaments are threaded by helical fields, then the poloidal currents associated with those fields must connect to the larger scale magnetic field of the molecular cloud itself. The polarization signatures on these larger scales will be detectable once more sensitive submillimeter cameras (e.g. SCUBA-2) are built. Higher sensitivity is only one goal of the next generation of detectors; the most important advance will come with the elimination of the need to chop on the sky. This will enable observations of polarized emission from faint, relatively featureless dust structures on scales larger than the detector field of view.

The second extended test of helical field geometries can be made with high resolution, interferometric, mapping. The helical field geometry predicts that depolarization should persist down to very small scales. In practice, such maps are hard to interpret since current interferometers are limited to observations of cores where star formation is already occurring. Ideally, one would like to observe filaments at equally high resolution, but this goal is hindered by sensitivity limits and the filtering of large scale structure beyond some limit imposed by the spacing of the array. While sensitivity will continue to improve, the filtering effect is not so easily overcome where short spacings information is not present.

Perhaps the most immediately tangible way to further test helical field models is the obser-

vation of regions over a range of wavelengths. If one were to observe shorter wavelengths until sources become optically thick, then the measurements could be used as a depth probe of the magnetic field. Although grain effects can produce changes in polarization percentage (Hildebrand et al. 1999), changes in position angle are attributed to the magnetic field. If a field is indeed helical, the vectors should change orientation relative to a straight filament, from alignment with the filament axis to orthogonality as wavelength decreases. The future SOFIA polarimeter, operating below 200 μm will be particularly useful for testing this aspect of the models.

5. Summary

The polarization patterns observed in Orion B are dominated by orderly structure on scales at least as large as the areas mapped (with the possible exception of the LBS 23N region). This result can only be consistent with magnetic fields that are ordered on similar scales or larger. The filamentary clouds, NGC 2024 and LBS 23N, exhibit polarization patterns that are inconsistent with purely poloidal magnetic fields threading the filaments, or with fields simply threaded transversely to them. Curved field lines are necessary to model the polarization data in NGC 2024. The fact that the polarization pattern is symmetric about the dense ridge of cores suggests that there is a correlation between the presence of dense gas and the exhibited polarization pattern.

The polarization systematically decreases with intensity for all three regions mapped. This result is in agreement with Paper II, which notes depolarization toward the axis of the Integral-shaped Filament in OMC-3, as well as most submillimeter and millimeter observations of star-forming regions (see Weintraub, Goodman & Akeson (2000) for a review). This “polarization hole” effect is a *global* property of our maps, and not just a local phenomenon that occurs for a few pixels near the very brightest emission.

NGC 2071 is a massive core forming multiple protostars. Its polarization pattern is ordered and qualitatively similar to that of OMC-1, which is an even more massive core in Orion A. In OMC-1, Schleuning (1998) interpreted their polarization data as being due to an hourglass magnetic field,

with the field lines pinched due to the collapse of the core. This interpretation is consistent with the flattening observed along the inferred field lines in OMC-1. On the other hand, NGC 2071 does not show any flattening, which is inconsistent with an interpretation of the magnetic field threading this core as a dynamically significant hourglass field. We note that if the vectors of NGC 2071 were rotated to infer a net field direction, this direction would be *perpendicular* to the most powerful outflow in the region. Alternatively, our map could be interpreted as resulting from a field that is predominantly toroidal about the axis of symmetry. Although CO $J = 3 - 2$ emission can contaminate SCUBA 850 μm data, we estimate it can contribute a maximum of 1% of polarized emission when optically thick. Since much higher polarizations are measured, we conclude that the polarizations measured in NGC 2071 are dominated by dust emission. Application of the Chandrasekhar & Fermi method to this core yields a mean field strength estimate of 56 μG , and we find that half the magnetic energy is accounted for by the mean field component.

LBS 23N exhibits the least orderly polarization patterns of the three regions studied. Most of the polarization vectors are aligned in a north-south orientation, particularly to the east of the cores. The cores themselves are significantly depolarized. Near the southern boundary of the map, the vectors rotate by 90° to an east-west orientation. This abrupt change might be explained either by an extension of the Fiege & Pudritz model (see §4.2), or by a smaller filament orthogonal to the main filament. More data to the south of LBS 23N would be needed to distinguish between these possibilities.

The NGC 2024 ridge of cores presents the most interesting polarization data of this paper. The polarization is strong everywhere except the cores, which are significantly depolarized. Our map agrees very well with the 100 μm polarization data obtained with the KAO Stokes polarimeter (Dotson et al. 2000), even though these wavelengths likely probe different dust temperatures. Interestingly, the region between FIR 4 and FIR 5 exhibits diminished intensity but no polarization is detected there. We are able to successfully model the polarization pattern using a helical field geometry threading a curved filament. However, given

the overall geometry of the region – an H II region expanding into the molecular cloud in which the cores are embedded – we slightly prefer a model in which the ionization front has swept up the magnetic field and is now stretching it around the ridge of dense cores. Since this model contains an unpolarized filament, it may be oversimplified and a more complete, complex picture will include both the polarized ionization front and a polarized filament.

We note that our analysis of the NGC 2024 polarization data have been aided immensely by the existence of Zeeman maps of the line-of-sight field strength toward part of this region published by Crutcher et al. (1999). Unfortunately, very few regions have been successfully mapped using Zeeman splitting (Crutcher 1999). This is an area where future technological advances in instrumentation would greatly improve our understanding of magnetic fields in molecular clouds.

The authors would like to thank J. Greaves and T. Jenness for assistance during observing and with data reduction. We also extend thanks to our fellow members of this JCMT key project, particularly C. Wilson and R. Pudritz for feedback on this manuscript, and our referee for a thorough and insightful review. The research of BCM has been supported through grants from the Natural Sciences and Engineering Research Council of Canada. BCM acknowledges funding from Ontario Graduate Scholarships. JDF acknowledges support from a postdoctoral fellowship, jointly funded by the Natural Sciences and Engineering Council and the Canadian Institute for Theoretical Astrophysics.

REFERENCES

Aitken, D. K., Greaves, J. S., Crysostomou, A., Jenness, T., Holland, W. S., Hough, J. H., Pierce-Price, D., & Richer, J. 2000, *ApJ*, 534, 173

Alves, J., Lada, C.J., Lada, E.A., Kenyon S.J., Phelps, R., 1998, *ApJ*, 506, 292

Anthony-Twarog, B. J., 1982, *AJ*, 87, 1213

Aso, Y. et al. 2000, *ApJS*, 131, 465

Bally, J. 1982, *ApJ*, 261, 558

Bally, J., & Lane, A. 1982, ApJ, 257, 612

Barnes, P.J., Crutcher, R.M., Bieging, J.H., Storey, J.W.V., & Willner, S.P. 1989, ApJ, 342, 883

Bontemps, S., André, P., & Ward-Thompson, D. 1995, A&A, 297, 98

Butner, H. M., Evans, N. J., Mundy, L. G., Natta, A., & Randich, M. S. 1990, ApJ, 364, 164

Chandler, C. J., & Carlstrom, J. E. 1996, ApJ, 466, 338

Chandrasekhar, S., & Fermi, E. 1953a, ApJ, 118, 113

Chandrasekhar, S., & Fermi, E. 1953b, ApJ, 118, 116

Chernin, L.M., & Masson, C.R. 1992, ApJ, 396, L35

Chini, R., Krügel, E., Haslam, C. G. T., Lemke, R., Reipurth, B., Sievers, A., & Ward-Thompson, D. 1993, A&A, 272, L5

Chini, R., Reipurth, B., Ward-Thompson, D., Bally, J., Nyman, L.-Å., Sievers, A., & Billawala, Y. 1997, ApJ, 474, L135

Coppin, K. E. K., Greaves, J. S., Jenness, T., & Holland, W. S. 2000, A&A, 356, 1031

Crutcher, R.M., Henkel, C., Wilson, T.L., Johnston, K.J., & Bieging, J.H. 1986, ApJ, 307, 302

Crutcher, R. M., 1999, ApJ, 520, 706

Crutcher, R.M., & Kazès, I. 1983, A&A, 125, L23

Crutcher, R.M., Roberts, D.A., Troland, T.H., & Goss, W.M. 1999, ApJ, 515, 275

Dotson, J.L., Davidson, J., Dowell, C.D., Schleuning, D.A., & Hildebrand, R.H. 2000, ApJS, 128, 335

Dowell, C. D., Hildebrand, R. H., Schleuning, D. A., Vaillancourt, J., Dotson, J. L., Novak, G., Renbarger, T., & Houde, M. 1998, ApJ, 504, 588

Draine, B. J., & Weingartner, J. C. 1996, ApJ, 470, 551

Eislöffel, J. A&A, 354, 236

Fukuda, N., & Hanawa, T. 2000, ApJ, 533, 911

Fiege, J.D., & Henriksen R.N., 1996, MNRAS, 281, 1038

Fiege, J.D., & Pudritz, R.E. 2000a, MNRAS, 311, 85

Fiege, J.D., & Pudritz, R.E. 2000b, MNRAS, 311, 105

Fiege, J.D., & Pudritz, R.E. 2000c, ApJ, 534, 291

Fiege, J.D., & Pudritz, R.E. 2000d, ApJ, 544, 830

Gaume, R.A., Johnston, K.J., & Wilson, T.L. 1992, ApJ, 388, 489

Genzel, R. & Downes, D. 1977, A&AS, 30, 145

Genzel, R., & Downes, D. 1979, A&A, 72, 234

Gibb, A. G. 1999, MNRAS, 304, 1

Gibb, A. G., & Heaton, B. D. 1993, A&A, 276, 511

Girart, J.M., Ho, P.T.P., Rudolph, A.L., Estalella, R., Wilner, D.J., & Chernin, L.M. 1999, ApJ, 522, 921

Goldreich, P., & Kylafis, N.D. 1981, ApJ, 243, L75

Goodman, A. A., Jones, T. J., Lada, E. A., & Myers, P. C. 1995, ApJ, 448, 748

Greaves, J.S., Jenness, T., Chrysostomou, A.C., Holland, W.S., & Berry, D.S. 2000, in Imaging at Radio through Submillimeter Wavelengths, eds. J.G. Mangum & S.J.E. Radford, ASP-CS 217, 18

Greaves, J.S., Holland, W.S., & Ward-Thompson, D. 2001a, ApJ, 546, L53

Greaves, J.S., Holland, W.S., Jenness, T., Moriarty-Schieven, G., Chrysostomou, A., Berry, D.S., Murray, A.G., Nartallo, R., Ade, P.A.R., Gannaway, F., Haynes, C.V., Tamura, M., Momose, M., & Morino, J.-I. 2001b, MNRAS, submitted

Heiles, C., Goodman, A. A., McKee, C. F., & Zweibel, E. G. 1993, in *Protostars & Planets III*, ed. E. H. Levy and J. I. Lunine (Tucson, University of Arizona Press), 279

Heitsch, F., Zweibel, E.G., Mac Low, M.-M., Li, P., & Norman, M. 2001, ApJ, 561, 800

Hildebrand, R. H. 1988, QJRAS, 29, 327

Hildebrand, R.H., Dotson, J.L., Dowell, C.D., Platt, S.R., Schleuning, D., Davidson, J.A., & Novak, G. 1995, in ASP Conf. Ser. 73, Air-bourne Astronomy Symposium on the Galactic Ecosystem: From Gas to Stars to Dust (San Francisco: ASP), 97

Hildebrand, R.H., Dotson, J.L., Dowell, C.D., Schleuning, D.A., & Vaillancourt, J.E. 1999, ApJ, 516, 834

Holland, W. S., Greaves, J. S., Ward-Thompson, D., & André, P. 1996, A&A, 309, 267

Holland, W. S., Robson, E. I., Gear, W. K., Cunningham, C. R., Lightfoot, J. F., Jenness, T., Ivison, R. J., Stevens, J. A., Ade, P. A. R., Griffin, M. J., Duncan, W. D., Murphy, J. A., & Naylor, D. A. 1999, MNRAS, 303, 659

Houde, M., Phillips, T.G., Bastien, P., Peng, R., & Yoshida, H. 2001, ApJ, 547, 311

Kazès, I., & Crutcher, R.M. 1986, A&A, 164, 328

Johnstone, D., & Bally, J. 1999, ApJ, 510, L49

Johnstone, D., Fich, M., Mitchell, G.F., & Moriarty-Schieven, G. 2001, ApJ, 559, 307

Kylafis, N. 1983, ApJ, 267, 137

Lada C.J., Alves, J., & Lada, E.A., 1999, ApJ, 512, 250

Lada, E. A., Bally, J., & Stark, A.A. 1991a, ApJ, 368, 432

Lada, E. A., DePoy, D. L., Evans, N.J., & Gatley, I. 1991b, ApJ, 371, 171

Launhardt, R., Mezger, P. G., Haslam, C. G. T., Kreysa, E., Lemke, R., Sievers, A., & Zylka, R. 1996, A&A, 312, 569

Lazarian, A., Goodman, A.A., & Myers, P.C. 1997, ApJ, 490, 273

Lery, T., Henriksen, R.N., & Fiege, J.D., 1999, \aa , 350, 254

Lis, D.C., Menten, K. M., & Zylka, R. 1999, ApJ, 527, 856

Matthews, B.C., & Wilson, C.D. 2000, ApJ, 531, 868 (Paper I)

Matthews, B.C., & Wilson, C.D. 2001, ApJ, accepted (Paper IV)

Matthews, B.C., Wilson, C.D., & Fiege, J.D. 2001, ApJ, 562, 400 (Paper II)

Mezger, P. G., Chini, R., Kreysa, E., Wink, J. W., & Salter, C. J. 1988, A&A, 191, 44

Mezger, P. G., Sievers, A. W., Haslam, C. G. T., Kreysa, E., Lemke, R., Mauersberger, R., & Wilson, T. L. 1992, A&A, 256, 631

Mitchell, G. F., Johnstone, D., Moriarty-Schieven, G., Fich, M., & Tothill, N. F. H. 2001, ApJ, 556, 215

Moriarty-Schieven, G. H., Snell, R. L., & Hughes, V. A. 1989, ApJ, 347, 358

Motte, F., André, P., Ward-Thompson, D., & Bontemps, S. 2001, A&A, 372, 41

Mouschovias T. 1976, ApJ, 207, 141

Nagai, T., Inutsuka, S., Miyama, S.M., 1998, ApJ, 506, 306

Nakamura, F., Hanawa, T., & Nakano, T. 1993, PASJ, 45, 551

Ostriker, J., 1964, ApJ, 140, 1056

Padoan, P., Goodman, A.A., Draine, B., Juvela, M., Nordlund, Å., & Rögnvaldsson, Ö. 2001, ApJ, submitted

Purcell, E. M. 1979, ApJ, 231, 404

Richer, J. S., Hills, R. E., & Padman, R. 1992, MNRAS, 254, 525

Sanders, D. B., & Willner, S. P. 1985, ApJ, 293, L39

Schleuning, D.A. 1998, ApJ, 493, 811

Schleuning, D. A., Dowell, C. D., Hildebrand, R. H., Platt, S. R., & Novak, G. 1997, PASP, 109, 307

Schulz, A., Güsten, R., Zylka, R., & Serabyn, E. 1991, A&A, 246, 570

Snell, R. L., & Edwards, S. 1982, ApJ, 259, 608

Snell, R. L., Scoville, N., Sanders, D. B., & Erickson, N. R. 1984, ApJ, 284, 176

Takano, T., Stutzki, J., Fukui, Y., & Winnewisser, G. 1986, A&A, 167, 333

Tomisaka, K., Ikeuchi, S., & Nakamura, T. 1988, ApJ, 326, 208

Visser, A. E., Richer, J. S., Chandler, C. J., & Padman, R. 1998, MNRAS, 301, 585

Walther, D. M., Robson, E. I., Aspin, C., & Dent, W. R. F. 1993, ApJ, 418, 310

Ward-Thompson, D., Kirk, J. M., Crutcher, R. M., Greaves, J. S., Holland, W. S., & André, P. 2000, ApJ, 537, 135

Weintraub, D. A., Goodman, A. A., & Akeson, R. L. 2000, in *Protostars & Planets IV*, eds. Manings, V., Boss, A. P., & Russell, S. S. (Tuscon: University of Arizona Press), 247

Yu, K.C. et al. 2000, AJ, 120, 1974

A. Polarization Data

Tables 1, 2, and 3 present the polarization data for the regions NGC 2071, LBS 23N, and NGC 2024 respectively. Each table contains only those vectors plotted on Figures 1, 2, and 3. Positional offsets for NGC 2071 are from $\alpha_{J2000} = 05^{\text{h}}47^{\text{m}}5\overset{\text{s}}{.}16$ ($05^{\text{h}}44^{\text{m}}31\overset{\text{s}}{.}0$ in B1950) and $\delta_{J2000} = +00^{\circ} 21' 47\overset{\text{s}}{.}1$ ($+00^{\circ} 20' 45\overset{\text{s}}{.}0$ in B1950). The reference position for LBS 23N is $\alpha_{J2000} = 05^{\text{h}}46^{\text{m}}11\overset{\text{s}}{.}16$ ($05^{\text{h}}43^{\text{m}}37\overset{\text{s}}{.}0$ in B1950) and $\delta_{J2000} = -00^{\circ} 09' 13\overset{\text{s}}{.}0$ ($-00^{\circ} 10' 15\overset{\text{s}}{.}2$ in B1950). Finally the reference position for NGC 2024 is $\alpha_{J2000} = 05^{\text{h}}41^{\text{m}}44\overset{\text{s}}{.}1$ ($05^{\text{h}}39^{\text{m}}12\overset{\text{s}}{.}6$ in B1950) and $\delta_{J2000} = -01^{\circ} 54' 49\overset{\text{s}}{.}7$ ($-01^{\circ} 56' 15\overset{\text{s}}{.}0$ in B1950).

The columns in each table are: (1) the R.A. offset in arcseconds; (2) the DEC. offset in arcseconds; (3) the polarization percentage at that position; (4) the uncertainty in the polarization percentage; (5) the signal-to-noise ratio of the polarization percentage; (6) the polarization position angle; and (7) the uncertainty in the polarization position angle.

TABLE 1
NGC 2071 850 μ M POLARIZATION DATA

Δ R.A. ($''$)	Δ DEC. ($''$)	p (%)	dp (%)	σ_p	θ ($^{\circ}$)	$d\theta$ ($^{\circ}$)
-16.5	-67.5	5.56	1.07	5.2	63.8	5.5
10.5	-58.5	12.99	1.41	9.2	-14.7	3.1
1.5	-58.5	8.51	1.33	6.4	7.0	4.5
-7.5	-58.5	5.14	1.04	4.9	42.8	5.8
-25.5	-58.5	6.04	1.40	4.3	-47.7	6.7
-43.5	-58.5	6.64	1.31	5.1	-20.4	5.7
10.5	-49.5	10.04	1.31	7.7	-29.3	3.7
1.5	-49.5	5.25	0.90	5.8	18.8	4.9
-25.5	-49.5	4.73	0.87	5.4	-80.1	5.3
-43.5	-49.5	13.76	1.48	9.3	-8.0	3.1
-52.5	-49.5	7.48	1.29	5.8	22.0	5.0
10.5	-40.5	3.54	0.61	5.9	-16.1	4.9
-16.5	-40.5	8.00	0.48	16.6	-14.2	1.7
-25.5	-40.5	4.56	0.68	6.7	6.9	4.3
-34.5	-40.5	9.33	1.46	6.4	-19.2	4.5
-52.5	-40.5	15.03	1.40	10.7	-17.2	2.7
37.5	-31.5	9.70	1.41	6.9	46.9	4.2
28.5	-31.5	11.90	1.02	11.6	26.4	2.5
19.5	-31.5	3.11	0.59	5.2	-2.2	5.5
10.5	-31.5	2.49	0.35	7.1	13.0	4.1
-16.5	-31.5	2.73	0.35	7.9	47.0	3.6
46.5	-22.5	4.34	1.06	4.1	54.2	7.0
19.5	-22.5	1.77	0.34	5.2	-1.2	5.5
10.5	-22.5	2.48	0.23	10.7	26.1	2.7
1.5	-22.5	1.25	0.26	4.8	47.0	6.0
-7.5	-22.5	1.83	0.21	8.8	70.0	3.2
-16.5	-22.5	1.66	0.25	6.6	-85.7	4.4
-34.5	-22.5	5.31	0.88	6.0	21.6	4.7
-52.5	-22.5	8.94	0.83	10.8	49.6	2.7
37.5	-13.5	5.70	0.93	6.1	57.6	4.7
28.5	-13.5	2.46	0.57	4.3	37.1	6.6
19.5	-13.5	2.29	0.30	7.6	13.5	3.8
10.5	-13.5	1.28	0.21	6.0	18.6	4.7
1.5	-13.5	1.04	0.17	6.3	35.0	4.5
-7.5	-13.5	1.53	0.18	8.4	53.0	3.4
-34.5	-13.5	3.15	0.31	10.1	57.8	2.8
-43.5	-13.5	5.76	0.50	11.6	37.1	2.5
-52.5	-13.5	4.17	0.68	6.1	30.2	4.7
37.5	-4.5	4.77	0.97	4.9	18.0	5.8
10.5	-4.5	1.74	0.17	10.3	14.1	2.8
1.5	-4.5	1.09	0.10	11.2	29.7	2.5

TABLE 1—*Continued*

Δ R.A. ($''$)	Δ DEC. ($''$)	p (%)	dp (%)	σ_p	θ ($^{\circ}$)	$d\theta$ ($^{\circ}$)
−7.5	−4.5	1.14	0.09	13.3	55.8	2.2
−25.5	−4.5	1.20	0.19	6.2	55.5	4.6
−34.5	−4.5	2.64	0.26	10.2	75.3	2.8
−43.5	−4.5	6.45	0.60	10.7	37.7	2.7
−52.5	−4.5	7.21	0.69	10.4	13.9	2.8
37.5	4.5	8.08	0.81	10.0	24.3	2.9
28.5	4.5	2.78	0.39	7.2	−20.5	4.0
−7.5	4.5	1.24	0.15	8.3	61.8	3.4
−16.5	4.5	1.66	0.17	9.5	54.2	3.0
−25.5	4.5	1.44	0.22	6.7	44.0	4.3
−43.5	4.5	3.73	0.59	6.3	37.1	4.5
37.5	13.5	5.95	0.76	7.8	21.6	3.7
28.5	13.5	1.43	0.33	4.3	−15.0	6.7
19.5	13.5	3.03	0.25	12.4	−2.0	2.3
10.5	13.5	1.31	0.25	5.3	−2.7	5.4
−7.5	13.5	1.41	0.24	5.9	50.4	4.9
−16.5	13.5	1.47	0.20	7.3	58.9	3.9
−25.5	13.5	2.18	0.32	6.8	38.0	4.2
−34.5	13.5	5.23	0.44	12.0	21.3	2.4
−43.5	13.5	4.95	0.57	8.6	19.3	3.3
−52.5	13.5	5.38	0.84	6.4	16.8	4.5
46.5	22.5	8.81	1.23	7.2	28.4	4.0
37.5	22.5	3.78	0.65	5.8	25.3	4.9
19.5	22.5	2.73	0.29	9.3	29.7	3.1
10.5	22.5	1.31	0.29	4.5	26.9	6.4
1.5	22.5	2.42	0.32	7.4	74.1	3.8
−7.5	22.5	1.64	0.32	5.0	60.2	5.7
−16.5	22.5	2.35	0.33	7.1	61.0	4.0
−25.5	22.5	2.60	0.34	7.6	31.4	3.8
−34.5	22.5	3.45	0.55	6.3	21.2	4.5
−43.5	22.5	5.42	0.54	10.0	17.7	2.9
−52.5	22.5	9.78	0.68	14.4	17.8	2.0
46.5	31.5	11.95	1.13	10.6	27.9	2.7
37.5	31.5	6.91	0.72	9.6	26.4	3.0
19.5	31.5	4.49	0.86	5.2	52.1	5.5
10.5	31.5	4.60	0.80	5.8	17.6	5.0
−25.5	31.5	2.74	0.64	4.3	−0.8	6.7
−34.5	31.5	4.45	0.51	8.8	13.6	3.3
−43.5	31.5	6.17	0.83	7.5	−7.8	3.8
37.5	40.5	5.39	0.73	7.4	−84.2	3.9
19.5	40.5	4.60	0.83	5.5	0.8	5.2

TABLE 1—*Continued*

Δ R.A. ($''$)	Δ DEC. ($''$)	p (%)	dp (%)	σ_p	θ ($^{\circ}$)	$d\theta$ ($^{\circ}$)
1.5	40.5	6.54	0.79	8.2	14.3	3.5
−34.5	40.5	3.77	0.78	4.8	43.7	5.9
−43.5	40.5	9.15	0.97	9.4	17.7	3.0
1.5	49.5	8.38	1.12	7.5	17.0	3.8
−7.5	49.5	7.30	1.04	7.0	14.0	4.1
−16.5	49.5	9.14	0.96	9.5	50.5	3.0
−34.5	49.5	6.52	0.84	7.8	80.0	3.7
37.5	58.5	3.30	0.80	4.1	−38.6	7.0
28.5	58.5	5.63	0.71	7.9	15.2	3.6
19.5	58.5	4.63	0.73	6.3	25.0	4.5
1.5	58.5	6.19	1.22	5.1	18.3	5.7
−7.5	58.5	5.60	1.31	4.3	8.9	6.7
−16.5	58.5	8.65	1.01	8.5	19.5	3.4
−25.5	58.5	3.16	0.69	4.5	35.9	6.3
−34.5	58.5	3.84	0.91	4.2	33.1	6.8
19.5	67.5	14.62	1.33	11.0	64.9	2.6
10.5	67.5	10.32	1.19	8.7	36.5	3.3

TABLE 2
LBS 23N 850 μ M POLARIZATION DATA

Δ R.A. ($''$)	Δ DEC. ($''$)	p (%)	dp (%)	σ_p	θ ($^{\circ}$)	$d\theta$ ($^{\circ}$)
-9.0	-124.5	5.58	1.03	5.4	-29.1	5.3
15.0	-112.5	12.03	1.37	8.8	29.9	3.3
3.0	-112.5	4.29	0.60	7.1	38.4	4.0
-9.0	-112.5	1.83	0.30	6.1	-16.7	4.7
15.0	-100.5	11.75	1.25	9.4	5.1	3.1
3.0	-100.5	5.34	0.68	7.8	74.4	3.7
-9.0	-100.5	3.14	0.34	9.1	-82.0	3.1
-21.0	-100.5	2.88	0.30	9.7	-88.8	3.0
-33.0	-100.5	3.12	0.62	5.0	71.7	5.7
-45.0	-100.5	8.47	1.35	6.3	75.1	4.5
15.0	-88.5	8.27	1.12	7.4	-11.9	3.9
3.0	-88.5	4.88	0.68	7.1	-3.4	4.0
-9.0	-88.5	1.97	0.49	4.1	-88.2	7.1
-21.0	-88.5	2.94	0.50	5.9	29.4	4.9
-33.0	-88.5	3.77	0.76	5.0	71.7	5.7
-45.0	-88.5	5.28	1.28	4.1	51.7	6.9
27.0	-76.5	13.00	1.34	9.7	28.8	3.0
15.0	-76.5	5.45	0.80	6.9	21.6	4.2
3.0	-76.5	3.61	0.65	5.6	-26.6	5.1
-9.0	-76.5	6.55	0.57	11.5	-53.6	2.5
-21.0	-76.5	7.21	0.77	9.4	-42.3	3.1
-45.0	-76.5	12.16	1.20	10.2	7.8	2.8
27.0	-64.5	7.82	1.29	6.0	1.8	4.7
15.0	-64.5	3.21	0.63	5.1	10.3	5.6
-9.0	-64.5	2.52	0.47	5.4	-78.8	5.4
-21.0	-64.5	3.40	0.71	4.8	62.8	5.9
27.0	-52.5	12.61	1.01	12.5	8.1	2.3
15.0	-52.5	6.77	0.47	14.5	4.9	2.0
3.0	-52.5	1.47	0.26	5.7	16.3	5.0
-9.0	-52.5	2.61	0.23	11.5	5.2	2.5
-21.0	-52.5	2.09	0.42	5.0	50.1	5.7
-33.0	-52.5	3.51	0.67	5.3	0.6	5.4
27.0	-40.5	8.82	0.74	11.9	6.9	2.4
15.0	-40.5	2.61	0.37	7.1	32.3	4.1
3.0	-40.5	1.55	0.13	11.6	23.5	2.5
27.0	-28.5	6.18	1.06	5.8	38.5	4.9
15.0	-28.5	5.57	0.41	13.5	28.3	2.1
3.0	-28.5	1.58	0.18	8.8	27.8	3.2
-9.0	-28.5	1.40	0.13	10.9	46.0	2.6
-21.0	-28.5	1.98	0.24	8.4	7.9	3.4
-33.0	-28.5	5.60	0.63	8.9	-6.9	3.2

TABLE 2—*Continued*

Δ R.A. ($''$)	Δ DEC. ($''$)	p (%)	dp (%)	σ_p	θ ($^{\circ}$)	$d\theta$ ($^{\circ}$)
51.0	−16.5	8.44	1.14	7.4	17.0	3.9
15.0	−16.5	7.53	0.92	8.2	29.0	3.5
3.0	−16.5	2.23	0.41	5.5	11.5	5.2
−9.0	−16.5	1.47	0.30	4.9	36.3	5.9
−21.0	−16.5	2.83	0.36	7.9	15.6	3.6
−45.0	−16.5	12.59	1.23	10.2	30.8	2.8
39.0	−4.5	6.46	1.17	5.5	−4.9	5.2
15.0	−4.5	21.96	1.30	16.8	−4.4	1.7
3.0	−4.5	2.54	0.54	4.7	15.1	6.1
−33.0	−4.5	4.97	0.58	8.6	−29.4	3.3
39.0	7.5	4.09	0.77	5.3	29.8	5.4
27.0	7.5	8.46	1.11	7.7	19.7	3.7
15.0	7.5	6.71	0.83	8.1	16.4	3.6
3.0	7.5	4.21	0.53	8.0	−28.8	3.6
−9.0	7.5	1.17	0.23	5.0	45.7	5.8
−21.0	7.5	1.26	0.28	4.5	−10.5	6.3
−33.0	7.5	3.28	0.50	6.5	20.0	4.4
39.0	19.5	11.24	1.09	10.3	−62.0	2.8
27.0	19.5	10.48	1.05	9.9	−30.8	2.9
15.0	19.5	5.70	0.58	9.8	21.4	2.9
3.0	19.5	4.01	0.44	9.2	−23.6	3.1
−9.0	19.5	5.57	0.43	12.9	14.6	2.2
−21.0	19.5	2.68	0.44	6.1	14.9	4.7
−33.0	19.5	7.10	0.43	16.4	−6.7	1.8
−45.0	19.5	1.89	0.46	4.1	26.3	7.0
3.0	31.5	5.46	0.66	8.2	57.2	3.5
−21.0	31.5	11.41	0.66	17.3	−4.8	1.7
−33.0	31.5	5.90	0.57	10.3	36.8	2.8
−45.0	31.5	7.10	0.78	9.1	11.6	3.2

TABLE 3
NGC 2024 850 μ m POLARIZATION DATA

Δ R.A. ($''$)	Δ DEC. ($''$)	p (%)	dp (%)	σ_p	θ ($^{\circ}$)	$d\theta$ ($^{\circ}$)
13.5	−147.0	6.77	1.13	6.0	−31.0	4.8
1.5	−147.0	4.99	0.90	5.5	−17.9	5.2
49.5	−135.0	9.39	0.93	10.1	−18.8	2.8
13.5	−135.0	4.28	0.38	11.3	−41.6	2.5
1.5	−135.0	5.81	0.32	18.2	−38.1	1.6
−10.5	−135.0	7.63	0.44	17.2	−24.5	1.7
−22.5	−135.0	8.92	0.90	9.9	51.7	2.9
49.5	−123.0	4.96	0.64	7.7	3.3	3.7
37.5	−123.0	5.35	0.60	8.9	−22.2	3.2
25.5	−123.0	1.87	0.32	5.8	−29.2	4.9
13.5	−123.0	4.50	0.15	29.7	−39.0	1.0
1.5	−123.0	4.03	0.27	15.2	−59.8	1.9
−10.5	−123.0	4.76	0.39	12.2	−46.0	2.3
−22.5	−123.0	3.95	0.50	8.0	−47.0	3.6
37.5	−111.0	3.12	0.37	8.5	−11.0	3.4
13.5	−111.0	1.94	0.19	10.2	−50.5	2.8
1.5	−111.0	2.05	0.30	6.8	−67.8	4.2
−10.5	−111.0	6.07	0.35	17.1	−33.0	1.7
−22.5	−111.0	3.07	0.42	7.3	−38.7	3.9
61.5	−99.0	9.10	0.90	10.1	−13.4	2.8
49.5	−99.0	4.27	0.37	11.6	−9.6	2.5
37.5	−99.0	1.37	0.26	5.4	23.6	5.4
13.5	−99.0	2.11	0.13	16.0	−35.9	1.8
1.5	−99.0	2.22	0.23	9.7	−41.3	3.0
−10.5	−99.0	1.96	0.29	6.8	−39.4	4.2
−34.5	−99.0	3.57	0.35	10.1	−60.2	2.8
−46.5	−99.0	2.18	0.47	4.7	81.4	6.1
−58.5	−99.0	5.21	1.08	4.8	−10.8	5.9
61.5	−87.0	3.55	0.42	8.4	9.3	3.4
49.5	−87.0	2.14	0.25	8.7	−8.7	3.3
37.5	−87.0	2.21	0.20	11.3	35.7	2.5
25.5	−87.0	1.11	0.15	7.5	33.0	3.8
13.5	−87.0	1.12	0.10	11.2	−33.3	2.6
1.5	−87.0	2.65	0.17	15.9	−27.0	1.8
−10.5	−87.0	2.38	0.19	12.3	−16.2	2.3
−22.5	−87.0	2.02	0.19	10.7	−24.0	2.7
−34.5	−87.0	1.47	0.33	4.5	−65.9	6.4
−46.5	−87.0	5.39	0.60	9.0	74.8	3.2
73.5	−75.0	7.90	0.98	8.0	−3.6	3.6
61.5	−75.0	4.94	0.35	13.9	−4.9	2.1
49.5	−75.0	2.70	0.19	14.4	10.1	2.0

TABLE 3—Continued

Δ R.A. ($''$)	Δ DEC. ($''$)	p (%)	dp (%)	σ_p	θ ($^{\circ}$)	$d\theta$ ($^{\circ}$)
37.5	-75.0	1.41	0.17	8.2	17.2	3.5
1.5	-75.0	1.31	0.12	10.5	-23.7	2.7
-10.5	-75.0	1.63	0.15	10.7	-20.7	2.7
-22.5	-75.0	1.77	0.16	10.8	-26.4	2.7
-34.5	-75.0	2.81	0.25	11.3	-10.2	2.5
-46.5	-75.0	3.50	0.52	6.8	-22.0	4.2
73.5	-63.0	5.45	0.99	5.5	-28.7	5.2
61.5	-63.0	4.26	0.35	12.3	5.7	2.3
49.5	-63.0	2.73	0.16	16.9	24.9	1.7
37.5	-63.0	1.38	0.14	10.0	7.6	2.9
1.5	-63.0	2.01	0.09	21.9	-48.0	1.3
-10.5	-63.0	1.27	0.12	10.6	-41.8	2.7
-22.5	-63.0	1.67	0.13	13.0	-19.0	2.2
-34.5	-63.0	3.24	0.21	15.7	-32.1	1.8
-46.5	-63.0	11.87	0.57	20.8	-43.6	1.4
73.5	-51.0	4.43	0.55	8.1	-7.3	3.5
61.5	-51.0	3.65	0.25	14.7	-0.6	2.0
49.5	-51.0	2.30	0.14	16.3	14.6	1.8
37.5	-51.0	1.33	0.09	14.0	20.9	2.0
25.5	-51.0	1.23	0.09	14.0	11.9	2.0
1.5	-51.0	1.42	0.04	32.4	-48.3	0.9
-22.5	-51.0	1.84	0.13	14.0	-52.1	2.0
-34.5	-51.0	3.01	0.27	11.2	-47.6	2.6
-46.5	-51.0	10.69	0.86	12.4	-60.8	2.3
73.5	-39.0	9.98	0.69	14.4	6.6	2.0
61.5	-39.0	3.22	0.24	13.3	3.7	2.2
49.5	-39.0	1.81	0.13	14.2	21.7	2.0
37.5	-39.0	1.20	0.10	11.5	34.7	2.5
25.5	-39.0	1.61	0.10	16.5	37.9	1.7
1.5	-39.0	1.02	0.09	11.8	-39.7	2.4
-10.5	-39.0	1.45	0.09	16.0	-50.1	1.8
-22.5	-39.0	2.14	0.19	11.6	-74.0	2.5
-34.5	-39.0	4.56	0.36	12.8	-74.1	2.2
-46.5	-39.0	6.39	0.63	10.2	-74.0	2.8
61.5	-27.0	2.27	0.30	7.5	3.5	3.8
49.5	-27.0	1.95	0.16	12.1	25.7	2.4
37.5	-27.0	2.24	0.14	16.5	34.0	1.7
25.5	-27.0	2.34	0.13	17.4	44.3	1.6
-10.5	-27.0	1.29	0.10	12.8	-72.7	2.2
-22.5	-27.0	2.53	0.18	13.9	-66.6	2.1
-34.5	-27.0	4.69	0.31	15.1	-80.7	1.9

TABLE 3—*Continued*

Δ R.A. ($''$)	Δ DEC. ($''$)	p (%)	dp (%)	σ_p	θ ($^{\circ}$)	$d\theta$ ($^{\circ}$)
-46.5	-27.0	4.83	0.35	13.9	-74.6	2.1
-58.5	-27.0	2.30	0.49	4.7	-47.5	6.1
73.5	-15.0	7.29	0.92	7.9	13.9	3.6
49.5	-15.0	1.39	0.19	7.3	25.1	3.9
37.5	-15.0	1.75	0.13	13.3	38.3	2.2
25.5	-15.0	1.93	0.14	14.1	36.9	2.0
-22.5	-15.0	1.45	0.16	9.1	-67.7	3.2
-34.5	-15.0	3.52	0.29	12.1	-67.8	2.4
-46.5	-15.0	1.35	0.28	4.9	-82.1	5.9
-58.5	-15.0	3.81	0.50	7.6	-85.3	3.8
73.5	-3.0	6.76	0.96	7.0	29.1	4.1
61.5	-3.0	4.65	0.47	10.0	34.9	2.9
49.5	-3.0	2.66	0.21	12.5	19.0	2.3
37.5	-3.0	2.44	0.15	16.8	37.7	1.7
25.5	-3.0	1.32	0.12	11.1	31.6	2.6
-10.5	-3.0	1.05	0.10	10.3	-61.8	2.8
-22.5	-3.0	2.08	0.13	16.5	-62.1	1.7
-34.5	-3.0	1.86	0.22	8.5	-84.5	3.4
-46.5	-3.0	3.92	0.33	12.1	-82.4	2.4
73.5	9.0	13.41	1.13	11.9	37.8	2.4
61.5	9.0	5.49	0.58	9.5	26.8	3.0
49.5	9.0	2.86	0.24	11.8	16.8	2.4
37.5	9.0	1.51	0.16	9.2	22.4	3.1
25.5	9.0	2.77	0.11	25.1	1.6	1.1
13.5	9.0	2.13	0.10	20.6	1.3	1.4
1.5	9.0	1.27	0.06	20.9	-23.8	1.4
-22.5	9.0	2.03	0.19	10.6	-67.1	2.7
-34.5	9.0	3.35	0.23	14.4	-76.1	2.0
-46.5	9.0	6.46	0.33	19.7	-87.7	1.5
-58.5	9.0	4.36	0.50	8.8	-62.4	3.3
49.5	21.0	2.54	0.36	7.0	22.0	4.1
37.5	21.0	1.89	0.21	9.2	2.2	3.1
25.5	21.0	3.32	0.14	24.5	-9.5	1.2
13.5	21.0	2.30	0.12	19.1	-1.0	1.5
1.5	21.0	1.98	0.13	15.1	3.2	1.9
-10.5	21.0	1.35	0.08	17.7	-28.7	1.6
-22.5	21.0	1.19	0.13	8.9	-43.9	3.2
-34.5	21.0	4.46	0.23	19.6	-79.7	1.5
-46.5	21.0	4.14	0.28	14.6	-69.5	2.0
-58.5	21.0	2.91	0.35	8.4	-89.4	3.4
49.5	33.0	4.16	0.77	5.4	-75.3	5.3

TABLE 3—*Continued*

Δ R.A. ($''$)	Δ DEC. ($''$)	p (%)	dp (%)	σ_p	θ ($^{\circ}$)	$d\theta$ ($^{\circ}$)
37.5	33.0	2.35	0.34	6.9	-26.5	4.2
25.5	33.0	3.73	0.25	15.1	-2.8	1.9
13.5	33.0	2.21	0.20	11.1	1.1	2.6
1.5	33.0	2.69	0.15	18.1	4.1	1.6
-10.5	33.0	1.63	0.17	9.9	-19.7	2.9
-22.5	33.0	1.80	0.07	25.5	-35.0	1.1
-34.5	33.0	2.56	0.24	10.5	-81.5	2.7
-46.5	33.0	1.32	0.23	5.6	-68.4	5.1
-58.5	33.0	1.61	0.35	4.6	-84.0	6.2
37.5	45.0	4.28	0.51	8.3	-42.2	3.4
25.5	45.0	3.07	0.42	7.4	-8.3	3.9
13.5	45.0	1.23	0.29	4.3	29.2	6.7
1.5	45.0	1.06	0.19	5.6	-25.6	5.2
-10.5	45.0	1.39	0.15	9.0	-28.6	3.2
-22.5	45.0	1.54	0.11	14.3	-24.8	2.0
-34.5	45.0	1.56	0.14	11.4	-82.5	2.5
-58.5	45.0	2.50	0.29	8.6	77.7	3.3
-70.5	45.0	6.64	1.16	5.7	52.6	5.0
25.5	57.0	6.36	0.61	10.4	-48.2	2.7
13.5	57.0	2.92	0.59	5.0	45.8	5.8
-22.5	57.0	1.29	0.25	5.2	-15.0	5.5
-34.5	57.0	1.50	0.14	10.4	-68.0	2.8
-46.5	57.0	1.28	0.21	6.0	-86.9	4.8
-58.5	57.0	3.11	0.49	6.3	46.3	4.5
49.5	69.0	7.34	0.83	8.8	52.7	3.3
37.5	69.0	6.92	0.78	8.8	32.4	3.2
25.5	69.0	9.29	0.76	12.3	-18.8	2.3
13.5	69.0	5.85	1.05	5.6	-72.8	5.2
1.5	69.0	3.52	0.44	7.9	-45.8	3.6
-22.5	69.0	2.00	0.21	9.4	-52.7	3.1
-46.5	69.0	1.92	0.23	8.3	86.5	3.4
13.5	81.0	5.06	0.45	11.3	-73.1	2.5
1.5	81.0	2.75	0.44	6.2	-32.5	4.6
-22.5	81.0	2.18	0.30	7.3	-36.2	3.9
25.5	93.0	4.15	0.55	7.5	23.1	3.8
1.5	93.0	2.70	0.63	4.3	-22.7	6.7

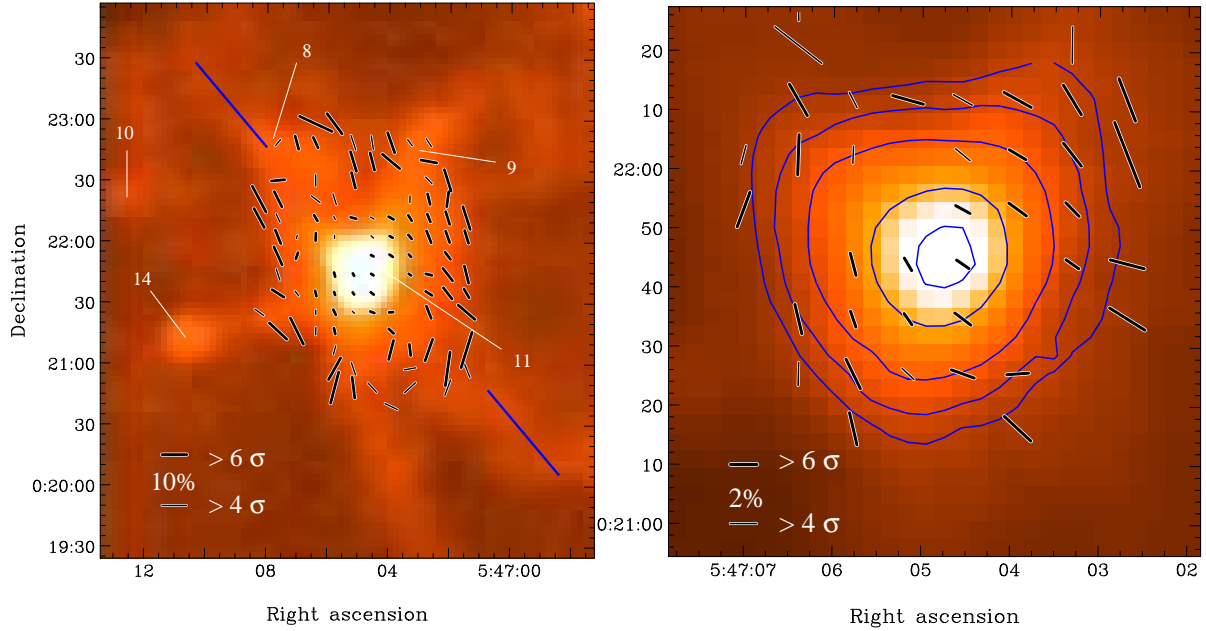


Fig. 1.— $850 \mu\text{m}$ polarization of NGC 2071. NGC 2071IR greyscale from (Mitchell et al. 2001) overlain with polarization vectors. The vectors are binned to 3 pixels ($9''$) so each vector is separated by just over half the $850 \mu\text{m}$ beamwidth ($14''$ at the JCMT). Vectors are only plotted where uncalibrated $I > 2\%$ of the source peak, polarization percentage exceeds 1% and the absolute uncertainty in polarization percentage is no greater than 1.5%. All vectors plotted have signal-to-noise in polarization percentage, $\sigma_p > 4$ (and therefore an uncertainty in position angle, $d\theta < 7.2^\circ$), but bold vectors have $\sigma_p > 6$ ($d\theta < 4.8^\circ$). Over the entire region, the mean position angle is 22° while the standard deviation is 32° . The mean polarization percentage is 5.1% with a standard deviation of 3.3%. Cores are labelled as in Mitchell et al. (2001), and blue lines mark the mean direction of the outflow from IRS 3. *Right:* Details of the central core (# 11 of Mitchell et al. (2001)) with the same vector cutoffs except $I > 12\%$ of the peak flux. Blue contours trace the surface density in unpolarized $850 \mu\text{m}$ intensity. All coordinates are J2000.

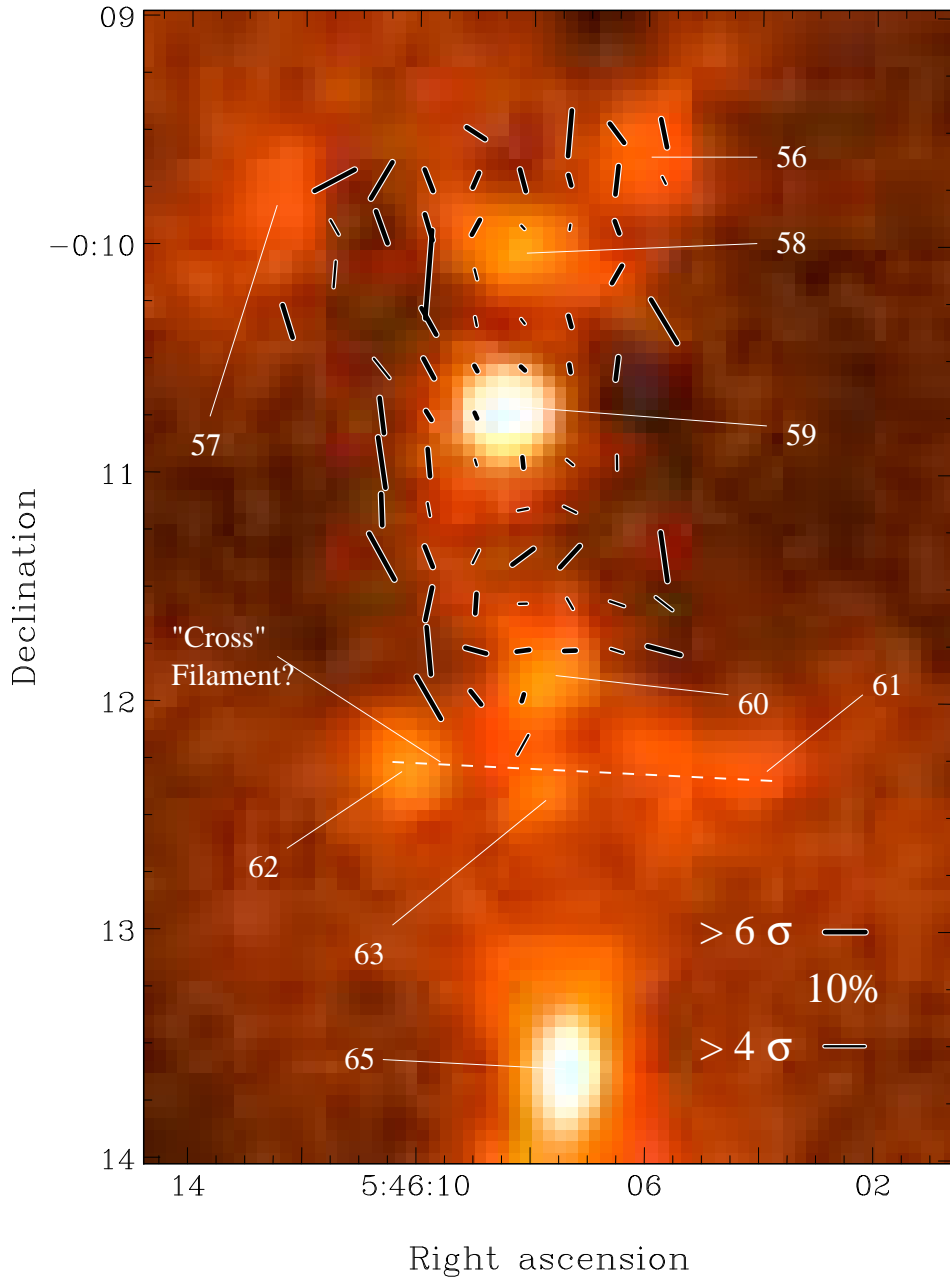


Fig. 2.— $850\text{ }\mu\text{m}$ polarization of LBS 23N. LBS 23 greyscale is taken from Mitchell et al. (2001). The polarization vectors overlaid have been binned to $12''$. Vectors are plotted where $I > 4\%$ of the peak of core 59, $p > 1\%$, $dp < 1.5\%$ and $p/dp > 4$ ($d\theta < 7.2^\circ$). Bold vectors show those where $p/dp > 6$ ($d\theta < 4.8^\circ$). The core identifications are taken from Mitchell et al. (2001). The mean polarization percentage measured is 5.6% with a standard deviation of 3.8%. A potential “cross” filament could be oriented east-west and has been indicated by the presence of a dashed line. Coordinates are J2000.

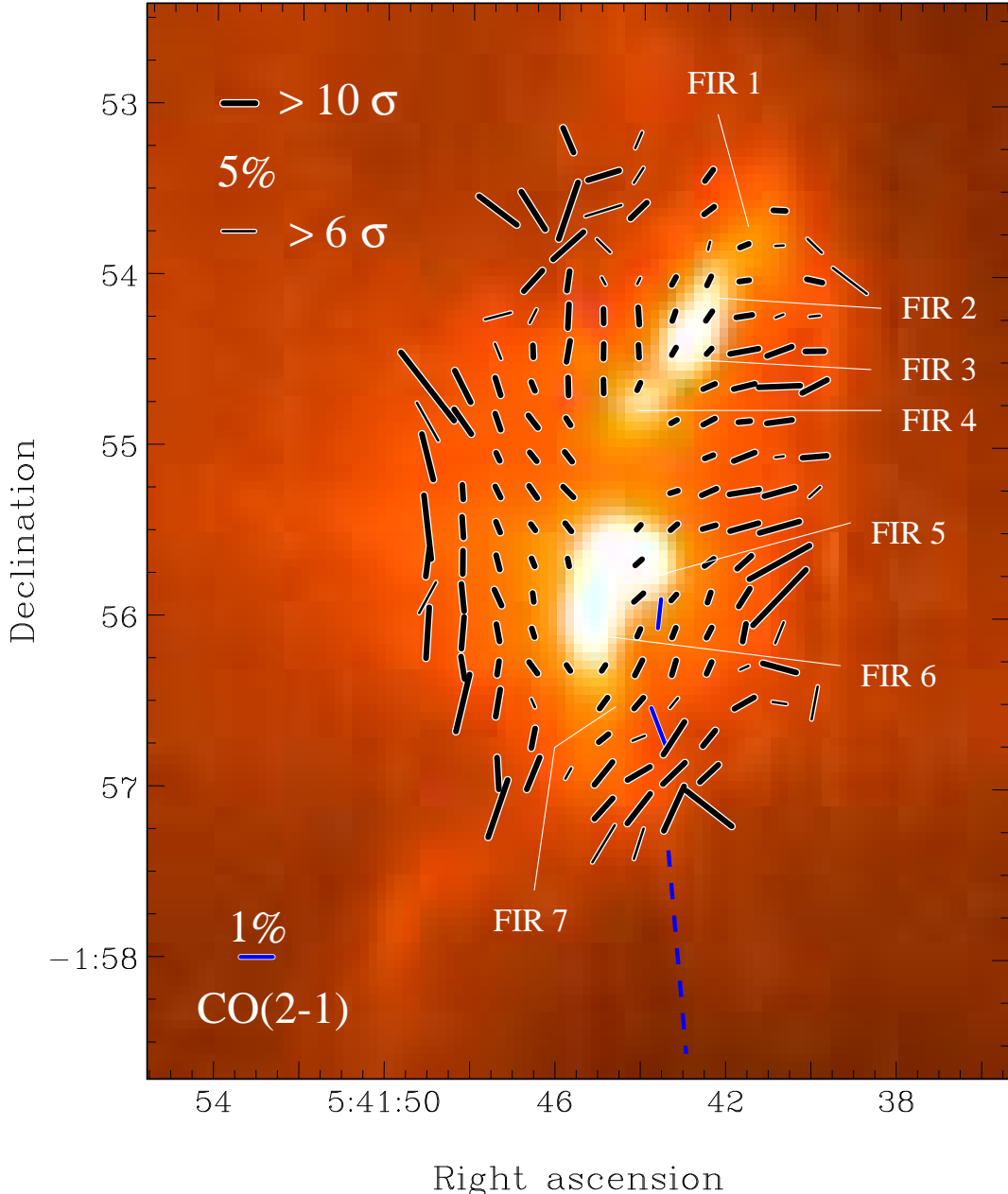


Fig. 3.— NGC 2024 850 μm polarization. NGC 2024 greyscale overlain with polarization 12'' binned polarization vectors, almost the JCMT beamwidth of 14'' at 850 μm . Vectors are plotted where $I > 2.5\%$ of the FIR 5 peak, $p > 1\%$, $dp < 1\%$ and $p/dp > 6$ ($d\theta < 4.8^\circ$). Bold vectors show those where $p/dp > 10$ ($d\theta < 2.9^\circ$). Overall, these data represent the highest signal to noise polarization detections in our data set. The mean percentage polarization is 3.4% with a standard deviation of 2.3% in 159 vectors. The submillimeter cores are labelled as in Mezger et al. (1988). We have indicated the orientation of the FIR 5 unipolar outflow by a blue dashed line, and the CO $J = 3 - 2$ line polarization vectors have been plotted (in blue) as measured by Greaves et al. (2001a). Coordinates are J2000.

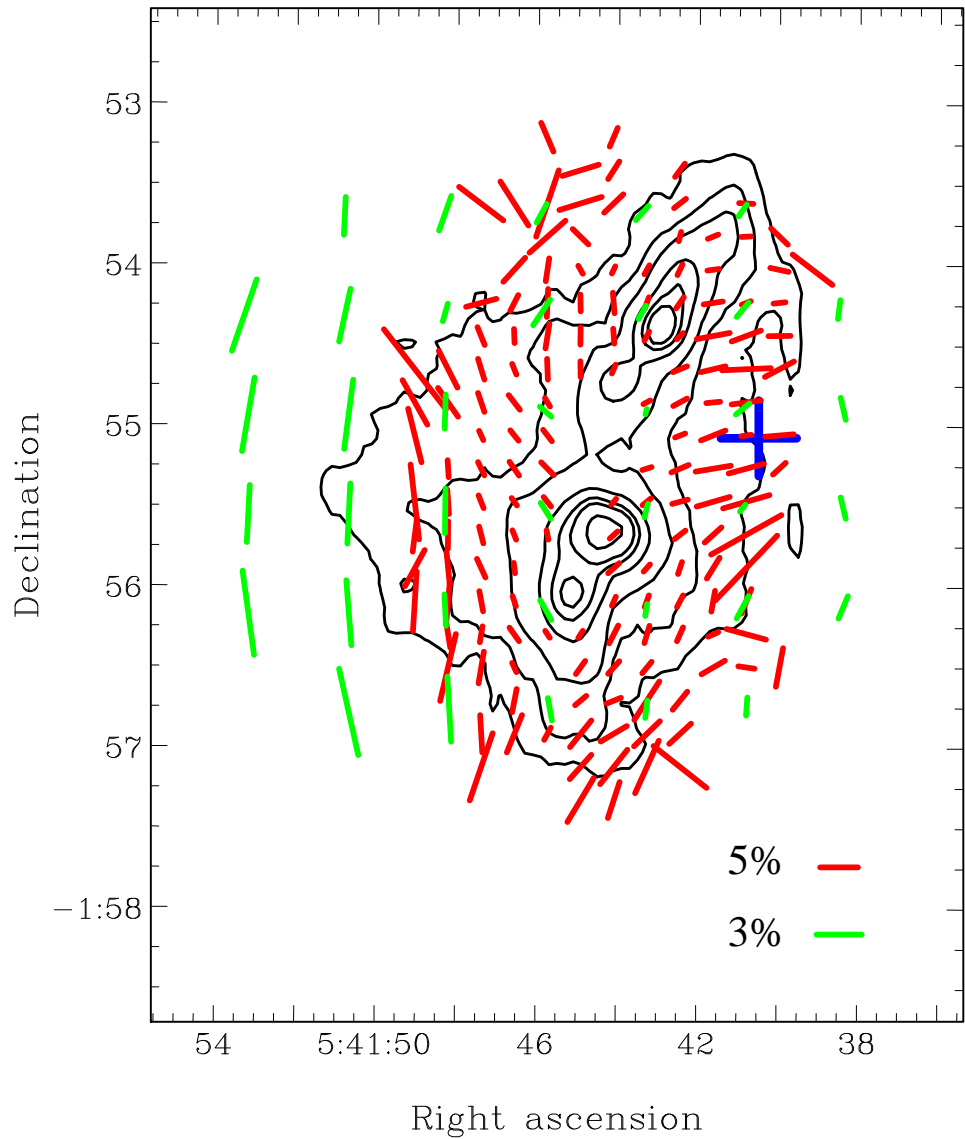


Fig. 4.— Comparison of Polarizations at $100 \mu\text{m}$ and $850 \mu\text{m}$. Comparison of the polarization patterns at $850 \mu\text{m}$ (red) and $100 \mu\text{m}$ (green) reveals a strong consistency in position angle. The polarization percentages are considerably lower for $100 \mu\text{m}$, possibly indicating that fewer dust grains are sampled within hotter dust or, more probably, that the dust grain alignment is lessened at higher temperatures. The $850 \mu\text{m}$ contours are plotted at 80, 90, 95, 98, 99, 99.5 and 99.9 percentiles. A blue cross marks the location of the maximum line-of-sight magnetic field as measured by Crutcher et al. (1999).

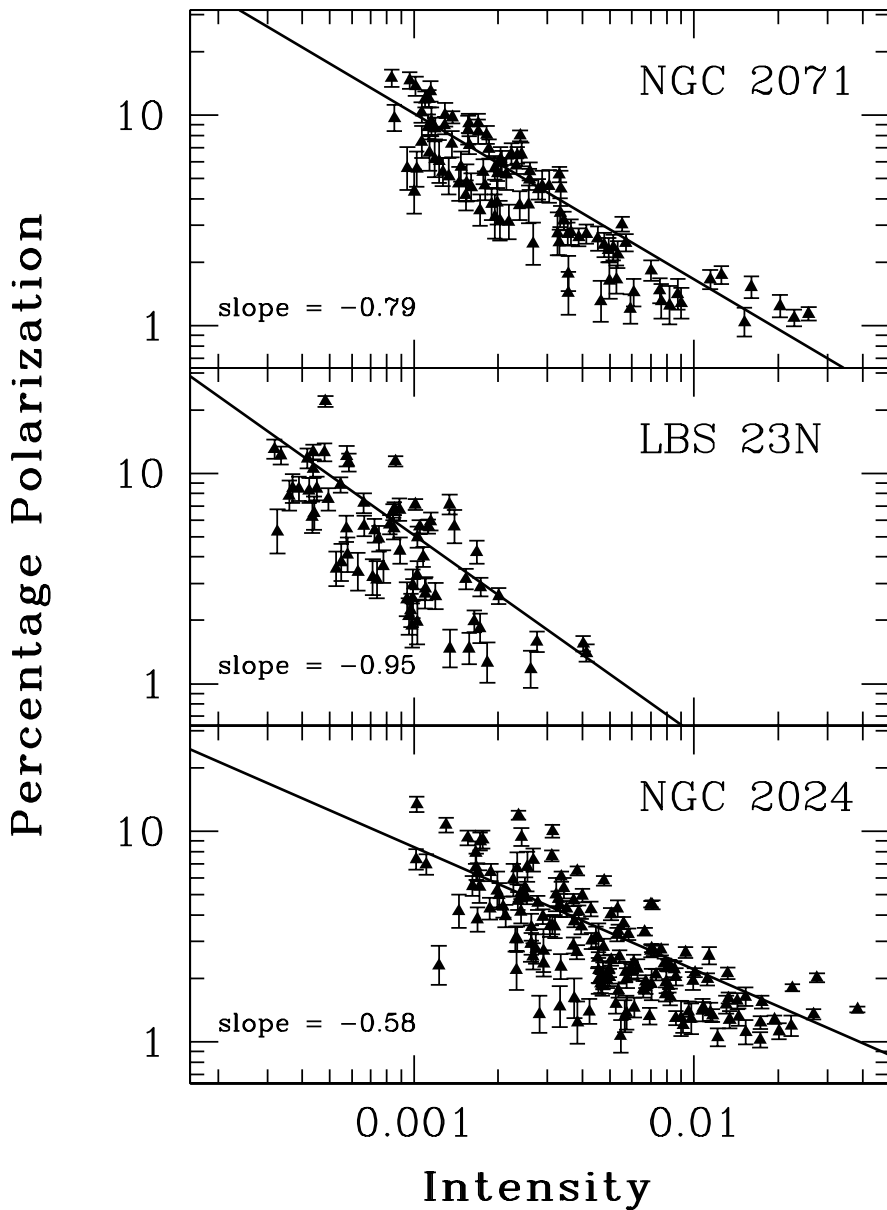


Fig. 5.— The Depolarization Effect in Orion B. The depolarization effect typically seen in protostars and extended regions (such as OMC-3 in Orion A) is also observed in NGC 2071, NGC 2024 and LBS 23N. For all three regions, the brightest positions have the smallest polarizations, exhibiting $< 2\%$ whereas the faintest regions show polarizations approaching and exceeding 10%. Decreased polarization percentage is observed for a large range of I values in NGC 2024. This region's cores also contain the largest areas where depolarization is total, or the levels of polarization are so low (i.e., $< 1\%$) as to be consistent with zero. Extremely high volume densities (on the order of 10^8 cm^{-3}) have been estimated in NGC 2024 (Mezger et al. 1988).

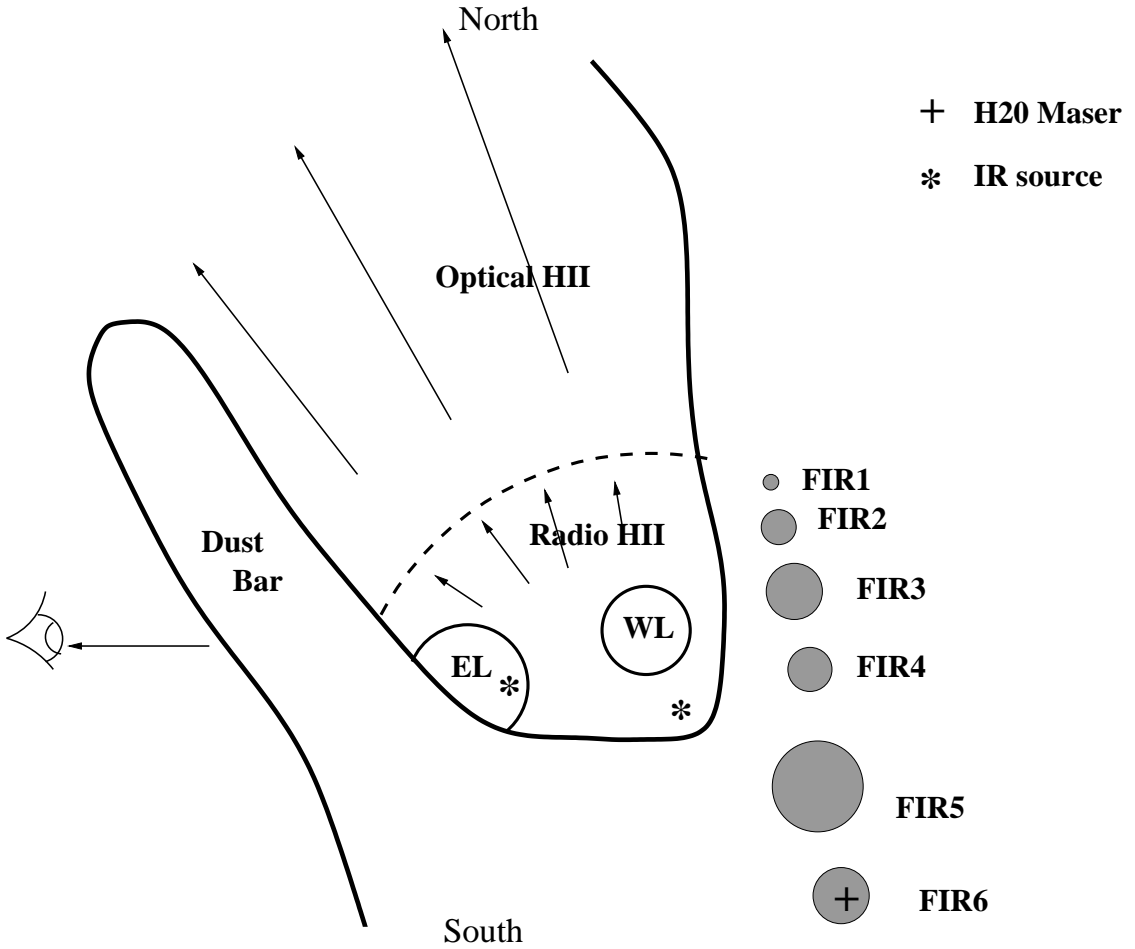


Fig. 6.— Schematic Geometry of the NGC 2024 region. The geometry of the NGC 2024 H II dense cores and foreground dark dust lane, as seen from the western edge of the cloud. From the Earth's perspective, the dark lane (unassociated with the dense cores) is seen in the foreground of the H II region. The H II region has blistered out of the molecular cloud to the north, west and east but is hindered to the south by dense molecular material as indicated by radio maps of the ionized emission (Barnes et al. 1989). The IR sources marked include IRS 2 (within the Eastern Loop) and IRS 3, near the southern boundary of the H II region.

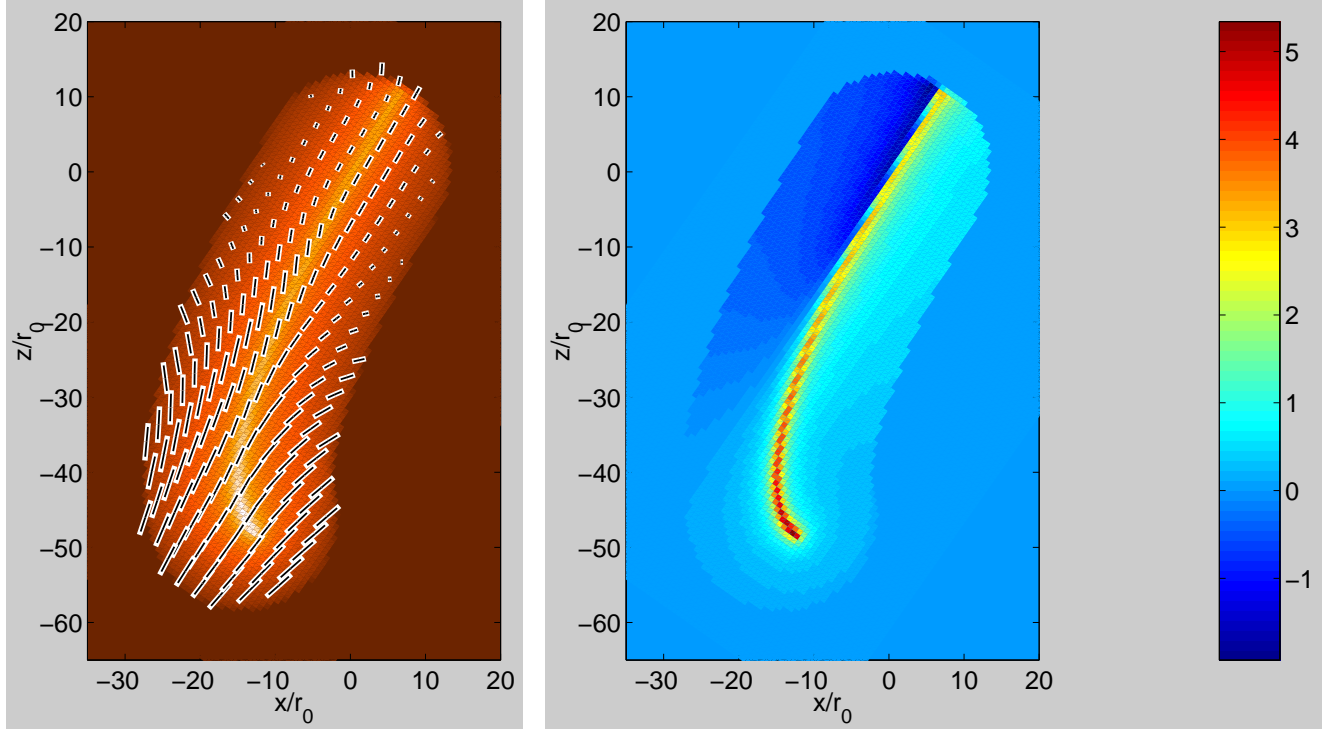


Fig. 7.— A Helical Field Model for NGC 2024. We show an example of a “bent filament” model (discussed in Section 4.3) for comparison with NGC 2024. The model is a Fiege & Pudritz (2000a) filament model constructed with the following parameters: $C = 1.1$, $\Gamma_z = 8$, $\Gamma_\phi = 15$. The length of the filament is 6×10^C and the ends have been rounded. We have bent the entire filament into a circular arc perpendicular to the plane of the sky and toward the observer, keeping the top of the filament parallel to the original orientation. The same pattern would be produced for a filament bent away from the observer. The radius of the arc is $3/\pi$ times the filament length. We then rotated the entire structure by 20° and inclined it relative to the plane of the sky by -15° . The right panel shows the expected line-of-sight field pattern from a helical field. A reversal in field direction is expected across the filament.

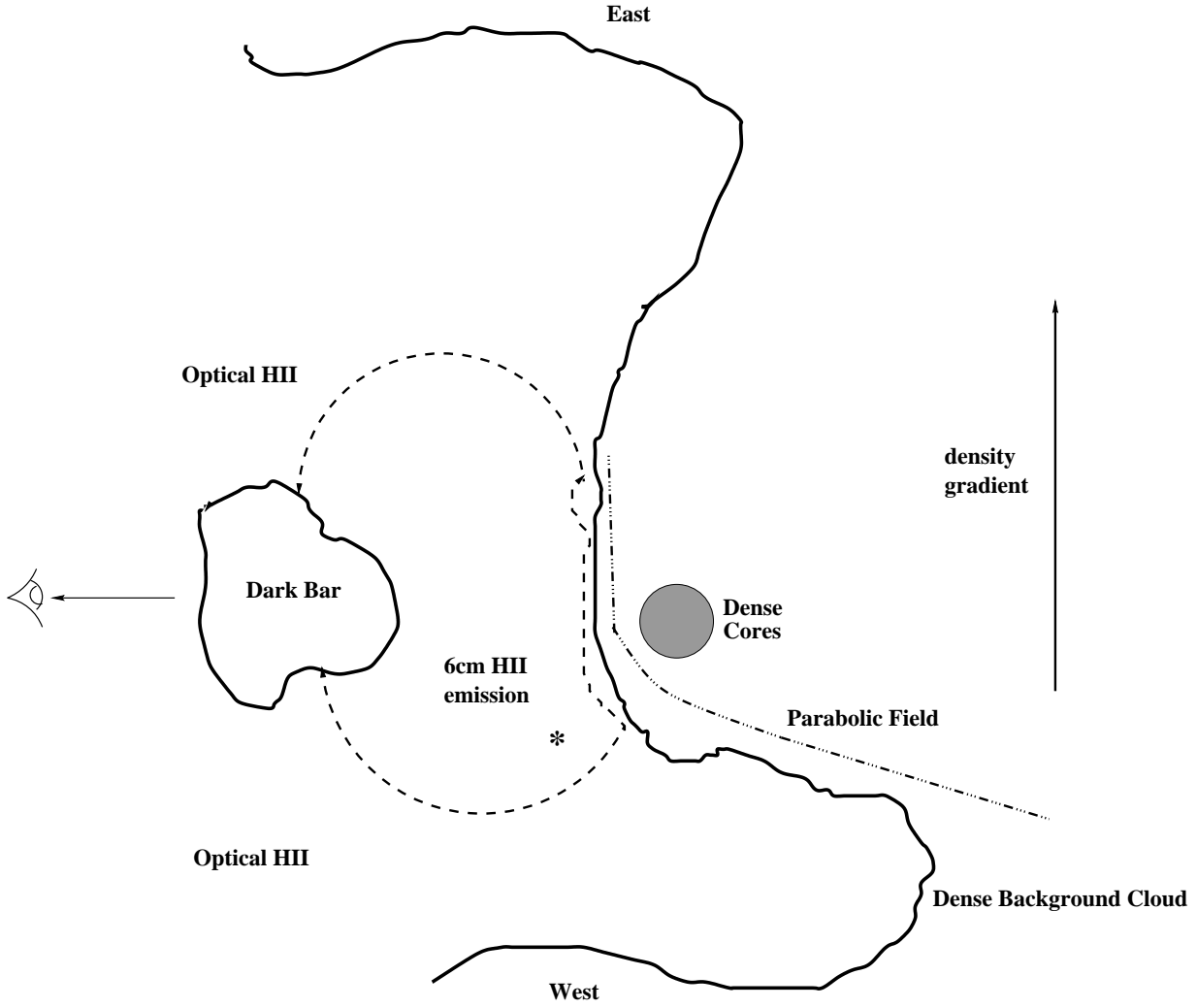


Fig. 8.— Geometry of the NGC 2024 region, viewed from the north. The geometry of the NGC 2024 region as viewed from the north, looking down on the ridge of dense cores. A proposed orientation of the field line is shown by the dot-dashed line. We speculate that the field has been compressed into a uniform layer on the edge of the expanding H II region. The ionization front has penetrated the molecular material more deeply to the west where the cloud is less dense, but is hindered by the dense ridge. This accounts for the field lying predominantly in the plane of the sky to the east of the ridge, but significantly in the line of sight to the west.

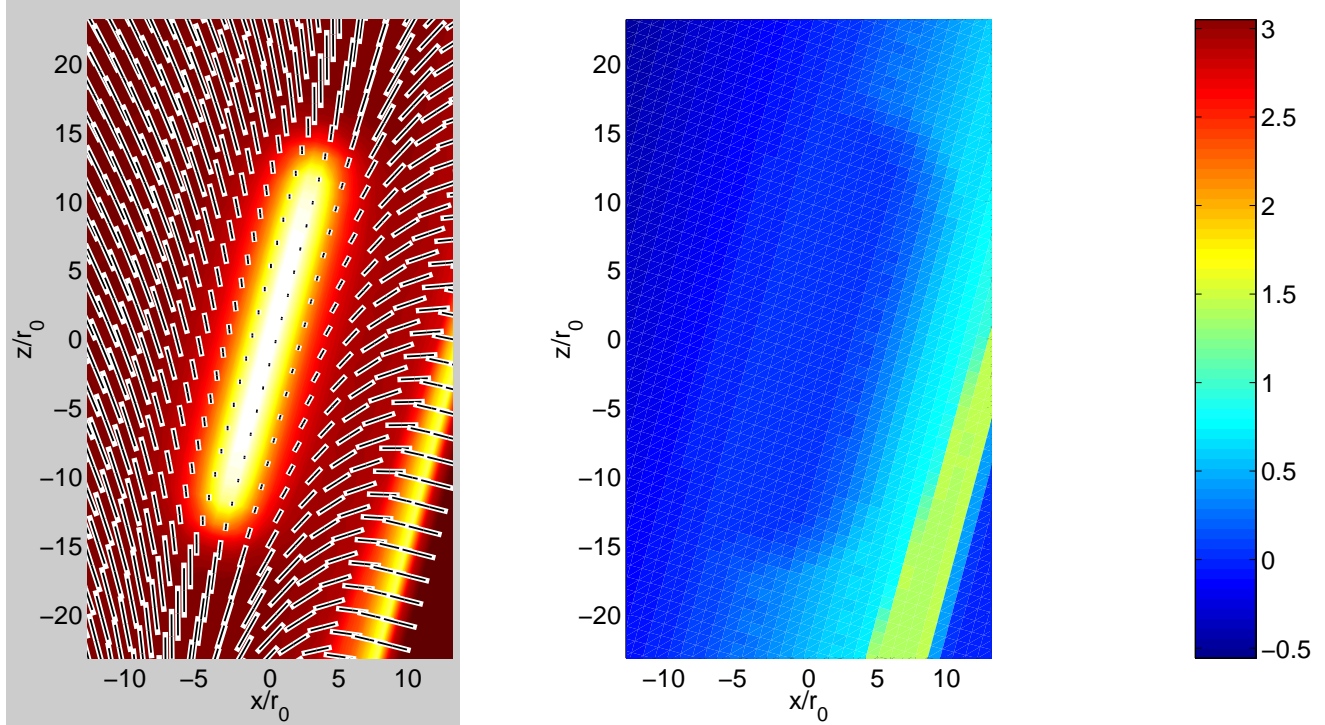


Fig. 9.— Polarization Pattern Produced by a Parabolic Field. Model showing the polarization pattern from a parabolic field bent around a dense ridge of gas, under the scenario depicted in Figure 8 and described in the text. The left panel shows the polarization pattern and the right traces the B_{los} . The filament is unmagnetized and the field is contained entirely in the shell of gas. The density of the shell containing the field must be $\sim 10\%$ that of the central axis of the filament. The parabolic shell is originally symmetric along the line of sight, but is rotated by 20° to produce the correct behavior in the polarization and B_{los} . The inclination is 60° and the whole filament is rotated by 15° on the plane of the sky.